Probing the transient dark state of substrate binding to GroEL by relaxation-based solution NMR

David S. Libich[a,1], Nicolas L. Fawzi[a,b,1], Jinfa Ying[a], and G. Marius Clore[a,2]

[a]Laboratory of Chemical Physics, National Institute of Diabetes and Digestive and Kidney Diseases, National Institutes of Health, Bethesda, MD 20892-0520; and [b]Department of Molecular Pharmacology, Physiology, and Biotechnology, Brown University, Providence, RI 02912

Edited* by George H. Lorimer, University of Maryland, College Park, MD, and approved May 20, 2013 (received for review March 25, 2013)

The mechanism whereby the prototypical chaperonin GroEL performs work on substrate proteins has not yet been fully elucidated, hindered by lack of detailed structural and dynamic information on the bound substrate. Previous investigations have produced conflicting reports on the state of GroEL-bound polypeptides, largely due to the transient and dynamic nature of these complexes. Here, we present a unique approach, based on combined analysis of four complementary relaxation-based NMR experiments, to probe directly the "dark" NMR-invisible state of the model, intrinsically disordered, polypeptide amyloid β (Aβ40) bound to GroEL. The four NMR experiments, lifetime line-broadening, dark-state exchange saturation transfer, relaxation dispersion, and small exchange-induced chemical shifts, are dependent in different ways on the overall exchange rates and populations of the free and bound states of the substrate, as well as on residue-specific dynamics and structure within the bound state as reported by transverse magnetization relaxation rates and backbone chemical shifts, respectively. Global fitting of all the NMR data shows that the complex is transient with a lifetime of <1 ms, that binding involves two predominantly hydrophobic segments corresponding to predicted GroEL consensus binding sequences, and that the structure of the bound polypeptide remains intrinsically and dynamically disordered with minimal changes in secondary structure propensity relative to the free state. Our results establish a unique method to observe NMR-invisible dynamic states of GroEL-bound substrates and to describe at atomic resolution the events between substrate binding and encapsulation that are crucial for understanding the normal and stress-related metabolic function of chaperonins.

supramolecular machine | protein–protein interactions | conformational sampling

Molecular chaperones are proteins that are ubiquitous to all three domains of life and assist native cellular proteins to reach their correct fate in vivo by facilitating folding, transport, oligomeric assembly, and controlled conformational switching (1–3). The chaperone system comprises a network of interconnected and redundant, yet unrelated, proteins that function via a broad range of mechanisms and under various physiological contexts. In addition to assisting in basal protein function, the chaperone system functions as a cellular quality control network tuned to mitigate the deleterious and toxic effects of environmental and pathological stress on proteins by preventing and, in some cases, reversing macromolecular aggregation (4). The energy barrier separating the folded and unfolded states is small for most proteins; consequently, many proteins are under continual risk of unfolding and aggregating, a risk that becomes particularly acute in response to extracellular stress. To carry out their protective role, chaperones have to interact transiently with myriad nonnative protein substrates to promote correct folding or assembly without the aid of stereospecific information on the native structure of the substrates. Generally, chaperones achieve this by presenting a hydrophobic surface that is able to bind exposed hydrophobic patches on partially folded or misfolded proteins (2, 3).

Chaperonins are a subclass of molecular chaperones characterized by cylindrical, stacked ring structures that form interior cavities large enough to encapsulate substrate proteins. The most studied and best understood chaperonin, both mechanistically and structurally, is GroEL, a 780-kDa supramolecular machine comprising seven identical 56-kDa subunits per cylindrical ring that assists protein folding through a multistep reaction cycle (2, 3). GroEL initially binds substrate proteins on exposed hydrophobic patches facing the inside of the cavity. Through a series of ATP-driven conformational rearrangements of the GroEL subunits and recruitment of the cochaperone GroES, GroEL encapsulates the substrate within the central chamber (2, 3). However, the structure and dynamics of substrate interactions with GroEL, as well as exactly how GroEL assists substrates to attain their native state (5–7), remain poorly understood, because the bound substrate, except under special circumstances, is generally invisible to conventional biophysical and structural techniques.

Previous investigations of GroEL have provided conflicting reports on the state of GroEL-bound peptides and proteins. Well-ordered β-hairpin and extended conformations have been observed by crystallography (8, 9), but these conformations were likely selected preferentially during crystallization. NMR-based transferred nuclear Overhauser enhancement studies have reported both helical and hairpin conformations (10–12), but interpretation is complicated by extensive spin diffusion (13) within GroEL. Conversely, hydrogen–deuterium exchange experiments (14, 15) imply that the secondary structure is sufficiently destabilized or disrupted upon binding to GroEL to allow substantial backbone amide hydrogen–deuterium exchange to occur. Likewise, ^{1}H-^{15}N correlation experiments, designed specifically for large (>>100 kDa) protein assemblies, suggest that bound protein substrates are dynamic and largely unfolded, because the few cross-peaks observed are located at characteristic random coil positions (16, 17).

The majority of physical studies on GroEL–substrate interactions have been carried out on heterologous systems, an approach validated by the high degree of conservation of chaperonins across evolution (2, 3). To address the conformational preferences and dynamics of a GroEL-bound substrate directly at atomic resolution, we have made use of four complementary relaxation-based NMR experiments (18–22) to probe directly and quantitatively the "dark" NMR-invisible state of the model, intrinsically disordered, polypeptide amyloid β (Aβ40) bound to GroEL. Although we use Aβ40 as a model system here to probe the interaction of intrinsically disordered, aggregation-prone proteins with GroEL, we note that the interaction of Aβ with the human homolog of GroEL, heat shock protein 60 (51% sequence identity), is involved in the translocation of Aβ to the mitochondria, where accumulation of Aβ plaques is thought to lead to mitochondrial dysfunction and to represent an important component of Alzheimer's disease (23).

Author contributions: D.S.L., N.L.F., J.Y., and G.M.C. designed research, performed research, analyzed data, and wrote the paper.

The authors declare no conflict of interest.

*This Direct Submission article had a prearranged editor.

[1]D.S.L. and N.L.F. contributed equally to this work.

[2]To whom correspondence should be addressed. E-mail: mariusc@mail.nih.gov.

This article contains supporting information online at www.pnas.org/lookup/suppl/doi:10.1073/pnas.1305715110/-/DCSupplemental.

Results and Discussion

We used a unique multipronged approach, based on the combined analysis of four relaxation-based NMR experiments, to study the dynamic interaction of Aβ40 with GroEL at atomic resolution. Specifically, lifetime line-broadening (20), dark-state exchange saturation transfer (DEST) spectroscopy (21, 22), Carr–Purcell–Meinboom–Gill (CPMG) relaxation dispersion spectroscopy (18, 24), and quantitative interpretation of very small exchange-induced chemical shifts (19) report in different ways on the overall exchange rates and populations of the free and bound states of Aβ40, as well as on residue-specific dynamics and structure within the bound state as reported by transverse magnetization relaxation rate constants (R_2) and backbone chemical shift values, respectively.

ΔR_2 Measurements. Fig. 1*A* displays the difference in ^{15}N-R_2 values (^{15}N-ΔR_2) of 50 μM monomeric Aβ40 (21) in the presence and absence of GroEL. Line-broadening can arise from two sources: differences in chemical shifts between the free and bound states giving rise to chemical exchange line-broadening and lifetime line-broadening due to large R_2 values in the bound state, leading to rapid decay of magnetization (20). At a CPMG field of 550 Hz, exchange-induced line-broadening is virtually completely suppressed and the observed increases in ^{15}N-R_2 values arise almost exclusively from lifetime line-broadening. This is evident from the absence of any correlation between ^{15}N-ΔR_2 values and ^{15}N exchange-induced shifts (Fig. 2*E*), as well as from analysis of the CPMG relaxation dispersion data (see below), which indicate that the largest contribution of exchange line-broadening to the measured ^{15}N-ΔR_2 values is less than 0.5 s^{-1} (Fig. S1). The ^{15}N-ΔR_2 values are linearly dependent on the concentration of GroEL (up to the highest concentration of GroEL used in the study, 40 μM in subunits) (Fig. S2 *C* and *D*), reflecting the linear dependence of ^{15}N-ΔR_2 on the pseudo–first-order association rate constant, $k_{\mathrm{on}}^{\mathrm{app}}$, given by $k_{\mathrm{on}}^{\mathrm{app}} = k_{\mathrm{on}}[\mathrm{GroEL}]_{\mathrm{free}} \approx k_{\mathrm{on}}[\mathrm{GroEL}]_{\mathrm{total}}/([\mathrm{A}\beta40]_{\mathrm{total}}\,K_{\mathrm{A}} + 1)$, where k_{on} is the second order association rate constant and K_{A} is the equilibrium association constant. In contrast to our previous

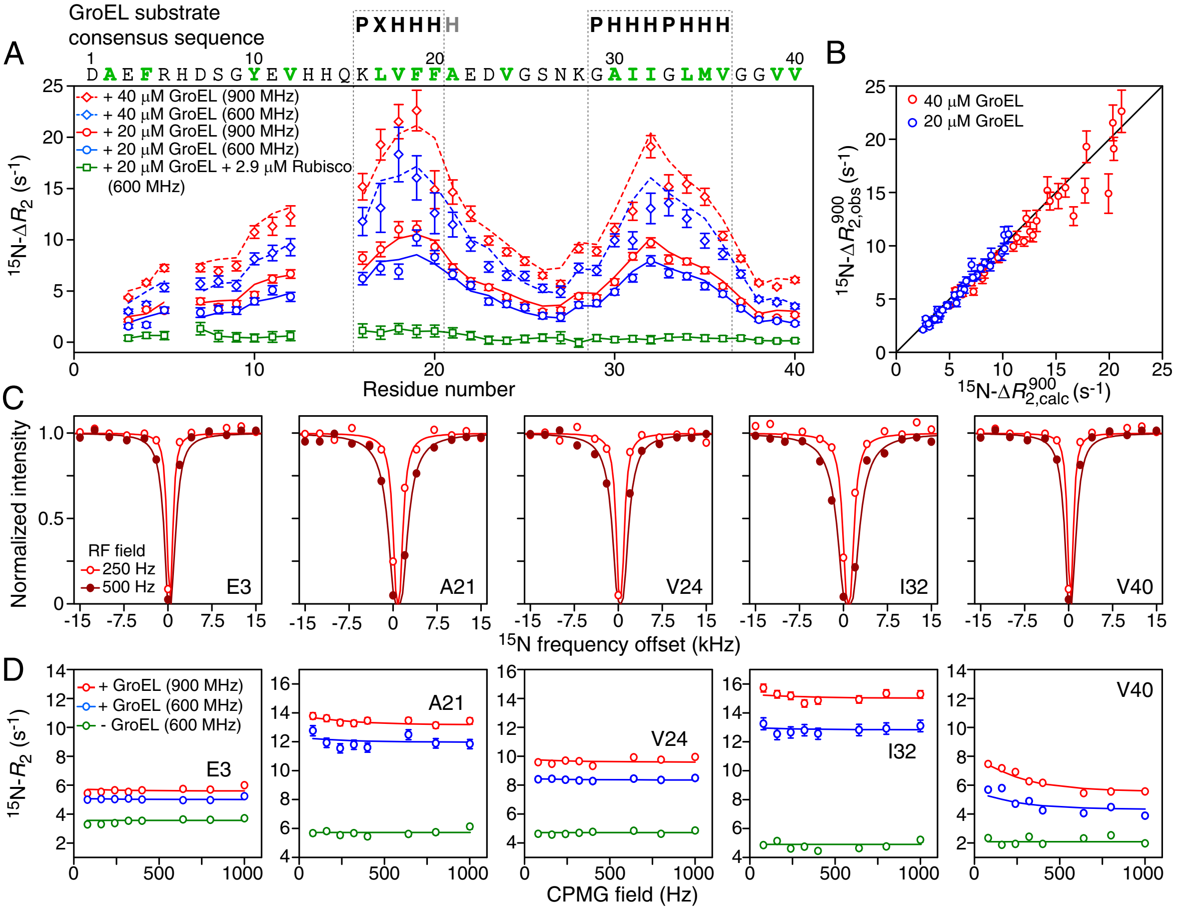

Fig. 1. ^{15}N-ΔR_2, ^{15}N-DEST, and ^{15}N relaxation dispersion profiles of Aβ40 in the presence of GroEL. (*A*) ^{15}N-ΔR_2 (CPMG field = 550 Hz) for 50 μM ^{15}N-labeled Aβ40 in the presence of 20 (circles) and 40 (diamonds) μM (in subunits) GroEL at spectrometer frequencies of 600 (blue) and 900 (red) MHz. ^{15}N-ΔR_2 at 600 MHz for a control sample (green squares) containing 50 μM ^{15}N-labeled Aβ40, 2.9 μM acid-denatured Rubisco, and 20 μM GroEL [in subunits, corresponding to 2.9 μM in Rubisco binding sites (i.e., one binding site per GroEL cavity)] demonstrates that acid-denatured Rubisco displaces GroEL-bound Aβ40. (*B*) Comparison of observed (obs) ^{15}N-ΔR_2 values with the calculated (calc) values obtained from global fitting of all experimental data to a two-state exchange model. (*C*) Examples of ^{15}N-DEST profiles (plotted as normalized cross-peak intensities as a function of frequency offset from the ^{15}N carrier at 118.5 ppm) obtained with rf (RF) field strengths of 250 (open circles) and 500 (closed circles) Hz for the ^{15}N continuous wave saturation pulse recorded at a spectrometer frequency of 900 MHz on a sample containing 50 μM ^{15}N-labeled Aβ40 in the presence of 20 μM (in subunits) GroEL. (*D*) ^{15}N-CPMG relaxation dispersion curves at spectrometer frequencies of 600 (blue) and 900 (red) MHz observed for 50 μM ^{15}N-labeled Aβ40 in the presence of 20 μM (in subunits) GroEL. Reference dispersion curves at 600 MHz for ^{15}N-labeled Aβ40 in the absence of GroEL are shown in green. The red and blue dashed and solid lines in *A* and *D* are the best-fit curves obtained by simultaneously fitting all the experimental data to a two-state exchange model. The green lines in *A* and *D* serve to guide the eye. The sequence of Aβ40 is shown at the top of the figure with hydrophobic residues highlighted in green and the GroEL substrate consensus sequences (where P stands for polar residues and H stands for hydrophobic residues) (28) aligned above the Aβ40 sequence for reference. All experiments were conducted at 5 °C. Error bars = 1 SD.

work on the interaction of monomeric Aβ40 on the surface of Aβ40 protofibrils, where ΔR_2 was found to be independent of the nucleus and magnetic field (20), the observed ΔR_2 profiles in the current study are dependent on the field (Fig. 1*A* and Fig. S2*B*) and nucleus (compare Fig. S2 *E* and *F*, which show that the ΔR_2 values for backbone amide protons are just over 50% larger than for ^{15}N). This immediately suggests that the dissociation rate constant, k_{off}, is of the same order of magnitude or larger than the R_2 values in the bound state (predicted to be $\sim$1,000 s^{-1} for ^{15}N at 5 °C and 900 MHz for a rigid N-H bond vector in a globular molecule the size of GroEL) and that $k_{\mathrm{on}}^{\mathrm{app}}$ must be greater than $\Delta R_2^{\mathrm{max}}$; otherwise, there would be no mechanism to create the observed residue-specific R_2 relaxation enhancement. Addition of acid-denatured ribulose-1,5-bisphosphate carboxylase (Rubisco) (25), a protein known to bind with high affinity specifically to the hydrophobic patches on the interior surface of the GroEL cavity, to a sample containing Aβ40 and GroEL reduces ^{15}N-ΔR_2 to values very close to zero (Fig. 1*A*), indicating that Rubisco and Aβ40 compete for the same binding site(s) on GroEL and that the lifetime line-broadening effect arises from a specific interaction of Aβ40 with GroEL.

^{15}N-DEST. Fig. 1*C* displays examples of ^{15}N-DEST profiles created by applying a weak ^{15}N saturation pulse at intervals from −21 to +21 kHz off-resonance of the spectrum of free Aβ40, thereby imprinting with single residue resolution dynamic information on the Aβ40 GroEL-bound species onto the easily observed ^{1}H-^{15}N correlation spectrum of free Aβ40 (21). When Aβ40 is bound to GroEL, reorientational motions within the peptide backbone of Aβ40 are dramatically slowed, resulting in ^{15}N-R_2 values that are several orders of magnitude larger than in the free state. Although these large ^{15}N-R_2 values preclude direct observation of the bound state, they allow for efficient partial saturation by a weak rf field even at large offsets, where the magnetization in the free state is completely unaffected, that is subsequently transferred back to the free state via chemical exchange and observed as a decrease in cross-peak intensity (21, 22). The profiles are dependent on k_{off}, and variations in width reflect residue-specific variations in ^{15}N-R_2 values in the bound state.

^{15}N-CPMG Relaxation Dispersion and Exchange-Induced Chemical Shifts. Fig. 1*D* provides some examples of ^{15}N-CPMG relaxation dispersion curves. Although no relaxation dispersion is observed in the absence of GroEL, small but clear-cut relaxation dispersion effects for some residues are apparent in the presence of GroEL. Relaxation dispersion is dependent on chemical shift differences between the free and bound states (24), and, interestingly, the largest dispersion is observed for the C-terminal residue Val40. Very small (≤1 Hz) but measurable exchange-induced chemical shifts are also observed for ^{15}N, ^{1}H$_{\mathrm{N}}$, ^{13}Cα, and ^{13}Cβ resonances (Fig. 2 *A* and *B*). The exchange-induced shifts are field-dependent (Fig. 2*C*) and directly proportional to the concentration of GroEL (Fig. 2*D*).

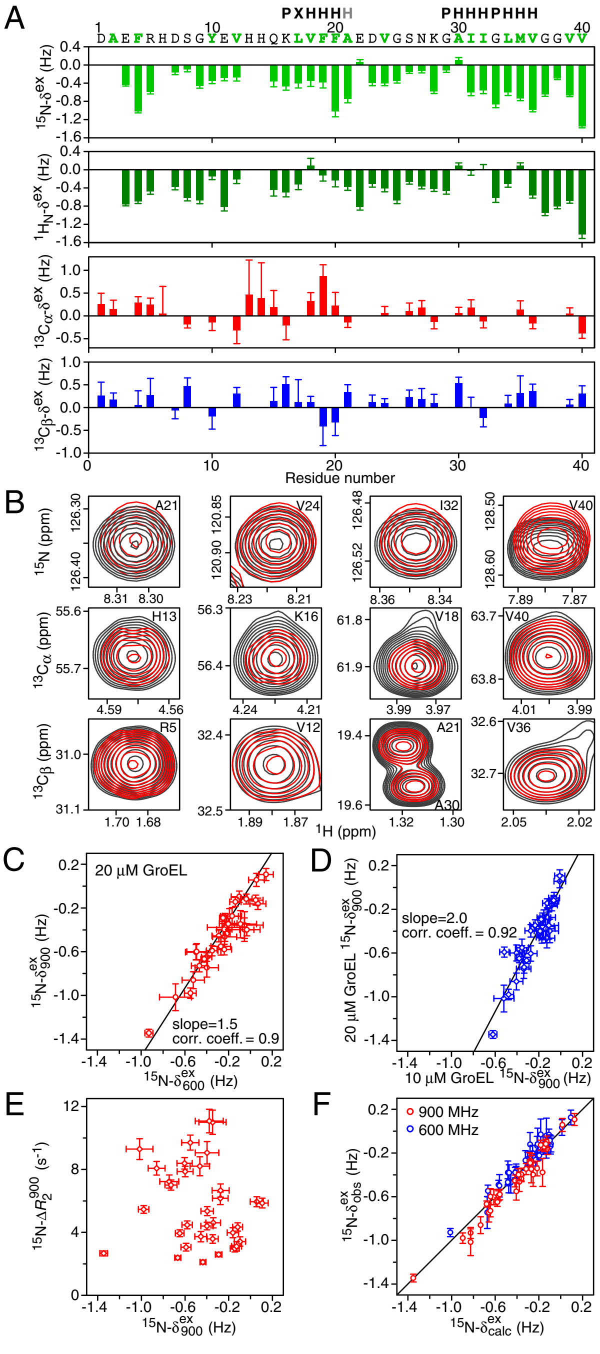

Fig. 2. Observed exchange-induced chemical shifts for Aβ40 in the presence of GroEL. (*A*) ^{15}N, ^{1}H$_{\mathrm{N}}$, ^{13}Cα, and ^{13}Cβ chemical shift differences (in hertz) between 50 μM ^{15}N-labeled Aβ40 samples containing 20 and 0 μM GroEL at a spectrometer frequency of 900 MHz. (*B*) Expansions of selected regions of the ^{1}H-^{15}N HSQC spectra and ^{1}H-^{13}C constant time HSQC spectra of 50 μM ^{15}N-labeled Aβ40 in the absence (black contours) and presence (red contours) of 20 μM GroEL. Correlation of ^{15}N exchange-induced chemical shifts of ^{15}N-labeled Aβ40 at two spectrometer frequencies (*C*) and two GroEL concentrations (*D*) is shown. corr. coeff., correlation coefficient. (*E*) ^{15}N-ΔR_2 values are not correlated to the ^{15}N exchange-induced chemical shifts. (*F*) Comparison of observed ^{15}N exchange-induced shifts with the calculated values obtained by simultaneously fitting all the experimental data to a two-state exchange model. Error bars = 1 SD.

Global Analysis of Relaxation-Based NMR Experiments. The data for all four relaxation-based NMR experiments at two fields (600 and 900 MHz) and several concentrations of GroEL were analyzed simultaneously using a simple two-state exchange model (Fig. 3*A*). All the experimental observables can be described by solutions to the McConnell equations (26) (*SI Materials and Methods*). The ^{15}N DEST profiles and ^{15}N-ΔR_2 values were calculated numerically (Eqs. S2 and S3), whereas analytical solutions were used for the ^{15}N relaxation dispersion data (Eqs. S4 and S5) and exchange-induced chemical shifts (^{15}N-δ^{ex}) (Eq. S6). Global nonlinear least-squares fitting (Eq. S7) was carried out by optimizing the values of two global parameters (whose values are determined by the data for all residues), namely, the pseudo–first-order association ($k_{\mathrm{on}}^{\mathrm{app}}$) rate constant and the fraction p_{A} of free Aβ40 [where the dissociation rate constant k_{off} is given by $k_{\mathrm{on}}^{\mathrm{app}} p_{\mathrm{A}}/(1-p_{\mathrm{A}})$, and the fraction p_{B} of GroEL-bound Aβ40 is given by $(1-p_{\mathrm{A}})$]; and two sets of residue-specific parameters, namely, ^{15}N-$R_{2,\mathrm{calc}}^{\mathrm{GroEL\text{-}bound}}(i)$ values in the bound state and the differences in ^{15}N chemical shift values, ^{15}N-$\Delta\delta(i)$, between the bound and free states, whose values are determined by the data for each individual residue. Comparisons of observed and calculated values for the ^{15}N-ΔR_2, ^{15}N-DEST, and ^{15}N relaxation dispersion curves are shown in Fig. 1 *A*, *C*, and *D*, respectively, and correlation plots between observed and calculated values for ^{15}N-ΔR_2 and ^{15}N-δ^{ex} are shown in Fig. 1*B* (also Fig. S2*A*) and Fig. 2*F*, respectively.

It is important to note that the combined use of all experiments is critical to finding the unique solution for the global kinetic parameters as well as the residue-specific ^{15}N-$R_{2,calc}^{GroEL\text{-}bound}(i)$ and ^{15}N-$\Delta\delta(i)$ values (*SI Materials and Methods*). The observables in each experiment have a unique dependence on the global and residue-specific parameters (compare Eqs. **S2**–**S6**). Thus, global fitting to a combination of observables using several orthogonal experiments not only results in a deeper minimum on the optimization landscape (critical in the presence of inevitable experimental uncertainty in the data) but, equally importantly, circumvents correlations in the values of the optimized parameters present in any one experiment (27) (further discussion is provided in *SI Materials and Methods*). Further, because there are only two global parameters, with the remaining parameters being entirely local to each residue position (and therefore uncorrelated from one residue to the next), the range of possible solutions in multidimensional parameter space is readily sampled.

The exchange model and global best-fit kinetic parameters are provided in Fig. 3*A*. At 20 µM (in subunits) GroEL, the population p_B of bound Aβ40 is 2.3 ± 0.1%, k_{on}^{app} has a value of 34.8 ± 0.8 s^{-1}, and k_{off} has a value of 1,440 ± 83 s^{-1}. Convergence of the solution was confirmed by varying initial values for all optimized parameters and obtaining the same solution within reported uncertainties. Assuming that one Aβ40 molecule binds per GroEL cavity, the value of the second-order association rate constant (k_{on}) is computed to be ~2 × 10^7 $M^{-1}\cdot s^{-1}$ and the value of the equilibrium dissociation constant (K_d) is ~70 µM. Alternatively, if we assume that it takes three Aβ40 molecules to saturate each cavity instead of one, and that the three Aβ40 molecules bind to each GroEL cavity completely independently from one another, the values of k_{on} and K_d are computed to be 4.7 × 10^6 $M^{-1}\cdot s^{-1}$ and 307 µM, respectively.

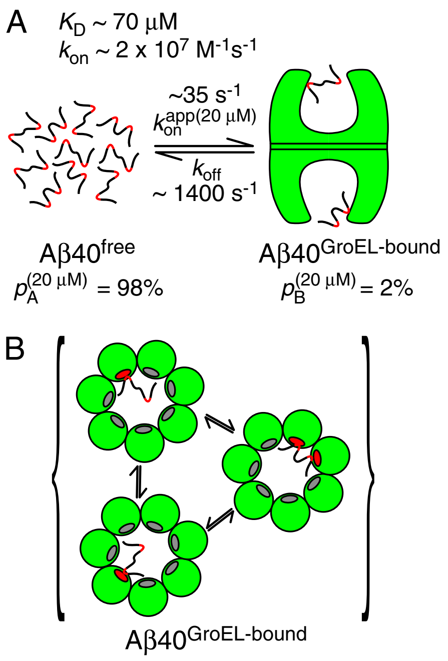

Fig. 3. Kinetic scheme for Aβ40 binding to GroEL. (*A*) Two-state exchange model describing the association of Aβ40 with GroEL. The values listed for k_{on}^{app} and the populations of free (p_A) and GroEL-bound (p_B) Aβ40 are those obtained in the presence of 20 µM GroEL. The equilibrium dissociation constant K_d and the second-order association rate constant k_{on} are calculated assuming each GroEL cavity only accommodates a single molecule of Aβ40 with numerous available binding modes. (*B*) Rapid interconversion (with a rate constant $>k_{off}$) between different GroEL-bound configurations of Aβ40 consisting of the central hydrophobic, C-terminal hydrophobic, or both hydrophobic regions in contact with GroEL is possible.

Residue-Specific ^{15}N-R_2 Values of Aβ40 in the GroEL-Bound State. The optimized values of ^{15}N-$R_{2,calc}^{GroEL\text{-}bound}(i)$ for Aβ40 bound to GroEL are shown in Fig. 4*A*. There are two regions that show particularly large ^{15}N-$R_{2,calc}^{GroEL\text{-}bound}$ values (350–650 s^{-1} at 900 MHz), namely, the central (residues 16–21) and C-terminal (residues 30–36) hydrophobic regions, which correspond to the GroEL-binding consensus sequences (28). With eight residues spanning the two hydrophobic regions, one would anticipate that the latter two segments of the polypeptide chain bind to adjacent subunits on GroEL. Thus, even if a single GroEL cavity can only accommodate one Aβ40 molecule, there are numerous potential binding modes: If we consider the central hydrophobic patch of Aβ40 first, each GroEL cavity has seven potential binding sites available, each with two adjacent sites available to bind the C-terminal hydrophobic patch (Fig. 3*B*). (Thus, the overall affinity can reach the micromolar range even if the individual contacts are much lower in affinity). The observation that the maximum ^{15}N-$R_{2,calc}^{GroEL\text{-}bound}$ value at 900 MHz is about 60–70% of the expected value for a rigid N-H group suggests that the two hydrophobic regions retain significant internal mobility on the nanosecond time scale when bound to GroEL and/or that the two hydrophobic regions bind to GroEL independently of one another. In the latter case, there would be two hemiassociated states in which only one hydrophobic region is in direct contact with GroEL at a given time, in addition to the fully bound state in which both hydrophobic regions are bound simultaneously. A third partially hydrophobic segment (Tyr-Glu-Val) from residues 10–12 displays intermediate ^{15}N-$R_{2,calc}^{GroEL\text{-}bound}$ values (~300 s^{-1} at 900 MHz), suggesting that this region may also transiently interact with GroEL, although to a lesser degree than the two main hydrophobic regions. The relatively low ^{15}N-$R_{2,calc}^{GroEL\text{-}bound}$ for the N and C termini (100–200 s^{-1}) suggests that these regions are significantly more mobile, and hence not in direct contact with GroEL but rather tethered to the surface of GroEL via the direct interactions between GroEL and the hydrophobic regions.

In contrast to the interaction of monomeric Aβ40 on the surface of Aβ40 protofibrils, where the bound state for each residue had to be kinetically partitioned between direct contact and tethered states (21), the current data are fully described by a simple two-state exchange model in which Aβ40 is either free or bound to GroEL. This implies that the interconversion rates between hemiassociated and fully associated states, as well as those between direct contact and tethered states for any given residue, are significantly faster than k_{off} (~1,400 s^{-1}).

Chemical Shifts and Structural Characteristics of Aβ40 in the GroEL-Bound State. The calculated differences in ^{15}N shifts (^{15}N-$\Delta\delta$) between bound and free Aβ40 are shown in the upper first panel of Fig. 4*B*. With only two exceptions (residues 21 and 30), all ^{15}N resonances are upfield-shifted in the bound state. The largest differences in ^{15}N shifts (−0.5 to −0.8 ppm) are observed for Phe20 and Ala21 in the central hydrophobic region; residues 31–36 (IIGLMV) within the C-terminal hydrophobic region; and, interestingly enough, three residues (Gly37, Val39, and Val40) at the C terminus. Indeed, the ^{15}N resonance of Val40 exhibits the largest chemical shift difference (~−0.8 ppm) between the bound and free states, as well as the largest relaxation dispersion (Fig. 1*D*, *Right*). Because the ^{15}N-$R_{2,calc}^{GroEL\text{-}bound}$ value for Val40 is low (~100 s^{-1}; Fig. 4*A*), this shift presumably arises through a secondary effect (e.g., through proximity to the bound C-terminal hydrophobic region).

Given the global exchange rate constants and the R_2 values in the GroEL-bound state, the ^1H_N, $^{13}C\alpha$, and $^{13}C\beta$ chemical shift differences ($\Delta\delta$) between the bound and free states can be computed from the observed exchange-induced shifts (δ^{ex}) using

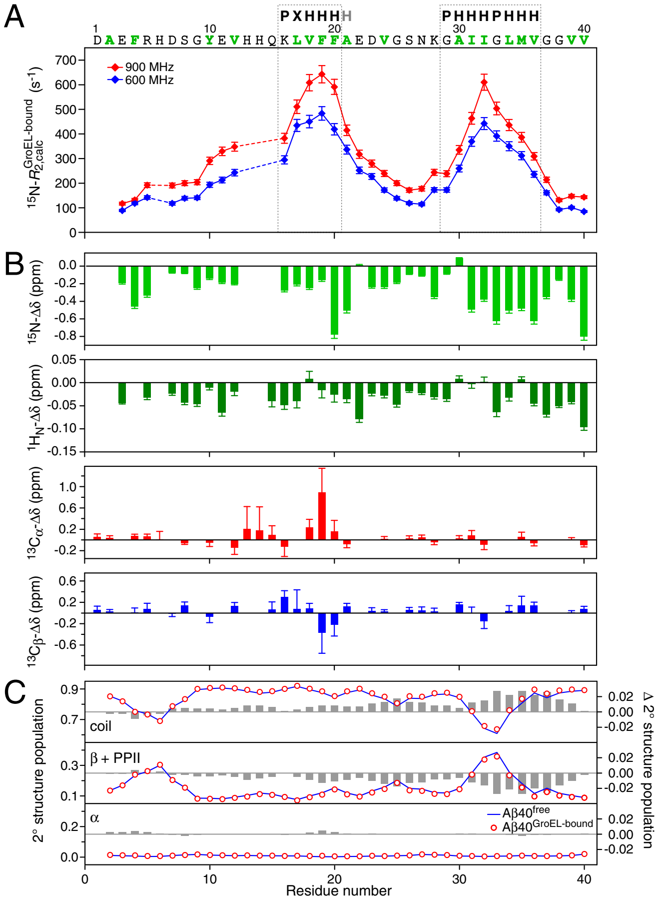

Fig. 4. Calculated residue-specific parameters for Aβ40 in the dark GroEL-bound state. (*A*) Optimized values of the residue-specific backbone ^{15}N-R_2 rates, ^{15}N-$R_{2,calc}^{GroEL\text{-}bound}(i)$, for GroEL-bound Aβ40 at spectrometer frequencies of 600 (blue) and 900 (red) MHz. (*B*) Residue-specific ^{15}N, ^{1}H$_N$, ^{13}Cα, and ^{13}Cβ chemical shift differences between GroEL-bound and free Aβ40. The ^{15}N chemical shift differences (^{15}N-Δδ) are optimized in the fitting procedure, whereas the other chemical shift differences are calculated from the ΔR_2 values and fitted global kinetic parameters (*SI Materials and Methods*). (*C*) Secondary structure populations (top, coil; middle, β and polyproline II; bottom, α) for free (blue line) and GroEL-bound (red circles) Aβ40 (*Left*, *y* axis) obtained using the δ2D method (29) and the difference in secondary structure populations between bound and free Aβ40 (gray bars; *Right*, *y* axis). Error bars = 1 SD.

Eq. S6. The results are displayed in the lower three panels of Fig. 4*B*. These backbone shifts allow one to ascertain quantitatively the structural characteristics of Aβ40 bound to GroEL. Although access to the chemical shifts of "invisible" bound states has been previously accessible from relaxation dispersion experiments alone (18, 24), it is important to note that incorporating quantitative interpretation of exchange-induced chemical shifts into the analysis provides the chemical shift difference (including the sign) at every observed position.

Free Aβ40 is largely random coil with only small β/polyproline II and α-helical propensities, as evidenced by the small deviations from the most recently published backbone chemical shift library for random coils (29) (Fig. S3) and the low values of the secondary structure propensities calculated from the backbone chemical shifts using the program δ2D (30) (Fig. 4*C*). The backbone ^{13}C chemical shifts induced on binding to GroEL are very small, with only the ^{13}Cα of Phe19 exhibiting a shift of greater than 0.4 ppm. The δ2D shift-based calculations indicate that the GroEL-bound state of Aβ40 is dynamically disordered, differing minimally from the intrinsically disordered free state. The GroEL-bound state exhibits a very small increase in helical propensity from residues 18–20 relative to the free state, consistent with the downfield ^{13}Cα and upfield ^{13}Cβ shifts for residues 19–20, perhaps indicative of a transient kink in the direction of the polypeptide chain. In addition, there appears to be a small overall increase in the coil population and a corresponding decrease in the β/polyproline II population on GroEL binding that is most marked in the C-terminal hydrophobic region, followed by residues 24–27 in the linker region and residues 17–21 in the central hydrophobic region.

Concluding Remarks. In summary, we have made combined use of four complementary relaxation-based NMR experiments, including a generally applicable method for extracting invisible state chemical shifts from quantitative interpretation of very small observed exchange-induced shifts, that, together, provide direct information at atomic resolution on the sparsely populated (~2%), NMR-invisible dark state of Aβ40 bound to GroEL. The data reveal that the primary sites of interaction with GroEL are located in two hydrophobic segments that coincide with the predicted GroEL consensus sequences (28) and indicate that Aβ40 remains intrinsically and dynamically disordered on binding to GroEL. We note that these two hydrophobic segments comprise the β-strand core of amyloid fibrils (31) and protofibrils (32), and are thus capable of forming a stable secondary structure (33). However, for the reasons discussed below, it is advantageous for GroEL function that substrates do not become ordered on binding.

The spacing between the two main hydrophobic regions suggests that these two segments bind to adjacent subunits of GroEL, and the ^{15}N-$R_{2,calc}^{GroEL\text{-}bound}$ values are suggestive of the existence of hemiassociated states in which only one of the two hydrophobic regions is in contact at a given time, as well as a state in which both segments are bound. Given the transient nature of the interaction, it is likely that Aβ40 exchanges between multiple pairs of sites within the cavity and that this exchange process occurs on a time scale that is faster (<700 μs) than the lifetime of the bound state.

The findings reported here provide a more complete description of GroEL–substrate interactions than was available from previous studies. Directly observed ^{1}H-^{15}N correlation methods were suggestive (but not conclusive) of protein substrates being disordered and dynamic while bound to GroEL, because all observable cross-peaks had chemical shifts characteristic of random coil and significant portions of the bound proteins were NMR-invisible because the cross-peaks for every residue type were underrepresented (16, 17). This conclusion, which was essentially one of exclusion because the portion of the protein substrates directly bound to GroEL could not be observed, is confirmed by the current work, which directly probes the NMR-invisible dark state of the bound substrate at every residue position. Further, conformational exchange of Aβ40 while bound to GroEL is also consistent with recent EM studies in which the substrate malate dehydrogenase was observed to adopt several binding topologies within the GroEL cavity (34).

The absence of structural ordering of Aβ40 on interaction with GroEL has important implications for the mechanism of substrate capture and release, because binding to GroEL likely entails minimal loss of entropy and extensive conformational plasticity that facilitates binding to essentially any solvent-exposed, 5- to 10-residue nonpolar sequence. Although binding to any individual hydrophobic segment may be very weak, the fact that multiple segments of a disordered polypeptide chain can bind to adjacent subunits of GroEL will result in a large increase in binding avidity, although still allowing for rapid dissociation. Further, the independent binding of multiple segments of Aβ40 may be indicative of a GroEL substrate selectivity mechanism for individual segments within a partially folded or misfolded ensemble. In the context of a kinetically trapped, partially folded or misfolded protein, it seems likely that initial binding of exposed hydrophobic segments will promote destabilization of the substrate, allowing the buried segments to become accessible for

GroEL binding, and thereby rapidly propagating the unfolding process. Moreover, binding to adjacent subunits within the cavity is likely to promote stretch-induced unfolding (35), followed by dissociation into the cavity, as the distance between binding sites on the apical domains of adjacent subunits is increased from ∼25 to ∼33 Å on transition from the closed state to ATP-bound open state (2). In the case of Aβ40, for example, the two GroEL-binding regions are separated by 14 residues center-to-center (Fig. 4*A*), which corresponds to an average end-to-end distance of 32–38 Å for a random coil calculated using well-established standard polymer theory (36) (*SI Materials and Methods*). Hence, the probability of the two hydrophobic regions of Aβ40 being bound to adjacent GroEL subunits simultaneously, and therefore the avidity of Aβ40 for GroEL, would be predicted to be higher in the closed state than in the open state.

In conclusion, the results presented here expand current paradigms of GroEL–substrate interactions by providing previously unobservable, residue-specific details of exchange kinetics, structure, and dynamics of polypeptides in the GroEL-bound dark state.

Materials and Methods

Uniformly ^{15}N-labeled Aβ40 was prepared from NaOH-treated stocks as described (20). *Escherichia coli* GroEL (37) and acid-denatured Rubisco (25) at natural isotopic abundance were purified as described previously and were a gift from George Lorimer and Don Yang (University of Maryland, College Park, MD). Aβ40 (50 μM) was combined with GroEL at 40, 20, 10, and 0 (reference sample) μM (in monomer units). An additional control sample was also prepared comprising Aβ40 (50 μM), GroEL (20 μM in monomer subunits), and Rubisco (2.9 μM). Sample conditions were 50 mM Hepes (pH 6.6) and 92% H_2O/8% D_2O. All samples were prepared and maintained at 5 °C at all times. Under these conditions, Aβ40 remains essentially entirely monomeric (>95%) for several weeks (21) (Fig. S4). NMR experiments were conducted at 5 °C on Bruker 900-MHz and 600-MHz spectrometers, each equipped with a triple-resonance, z-gradient cryoprobe.

The ^{15}N-R_2 (with a relaxation-compensated CPMG scheme at a CPMG field of 550 Hz to eliminate virtually all chemical exchange line-broadening) (20), ^{15}N-longitudinal magnetization relaxation rate R_1 (Fig. S5) (21), ^{15}N-$R_{1\rho}$ (Fig. S6) (38), ^{15}N-DEST (Fig. S7) (21), and ^{15}N-CPMG (single quantum) relaxation dispersion (39) experiments were carried out as described previously. ^{15}N and ^1H_N, as well as ^{13}Cα and ^{13}Cβ, exchange-induced shifts were measured from high-resolution ^{1}H-^{15}N heteronuclear single quantum coherence (HSQC) experiments and constant-time ^{1}H-^{13}C HSQC experiments, respectively (further details are provided in *SI Materials and Methods*).

All the DEST, ΔR_2, CPMG relaxation dispersion, and exchange-induced chemical shift data for ^{15}N were simultaneously fit to a two-state (free/bound) model (see Fig. 3) using a combination of numerical and analytical solutions to the McConnell equations (26) to determine the global kinetic parameters and the GroEL-bound ^{15}N-R_2 values and ^{15}N chemical shifts at each residue as described in *SI Materials and Methods* (Eqs. **S2**–**S7**). The GroEL-bound ^1H_N and ^{13}Cα/β shifts were determined from the corresponding exchange-induced shifts in conjunction with the R_2 rates and global kinetic parameters as described in *SI Materials and Methods*.

ACKNOWLEDGMENTS. We thank Dusty Baber and Dan Garrett for NMR technical assistance, Dennis Torchia and George Lorimer for valuable discussions, and George Lorimer and Dong Yang for their generous gift of GroEL and Rubisco. This study used the high-performance computational capabilities of the Biowulf Linux cluster at the National Institutes of Health (NIH). This work was supported by the intramural program of the National Institute of Diabetes and Digestive and Kidney Diseases, NIH, and by the AIDS Targeted Antiviral Program of the NIH Director (G.M.C.).

1. Hendrick JP, Hartl FU (1993) Molecular chaperone functions of heat-shock proteins. *Annu Rev Biochem* 62:349–384.
2. Thirumalai D, Lorimer GH (2001) Chaperonin-mediated protein folding. *Annu Rev Biophys Biomol Struct* 30:245–269.
3. Horwich AL, Fenton WA (2009) Chaperonin-mediated protein folding: Using a central cavity to kinetically assist polypeptide chain folding. *Q Rev Biophys* 42(2):83–116.
4. Saibil HR (2008) Chaperone machines in action. *Curr Opin Struct Biol* 18(1):35–42.
5. Todd MJ, Lorimer GH, Thirumalai D (1996) Chaperonin-facilitated protein folding: Optimization of rate and yield by an iterative annealing mechanism. *Proc Natl Acad Sci USA* 93(9):4030–4035.
6. Walter S, Lorimer GH, Schmid FX (1996) A thermodynamic coupling mechanism for GroEL-mediated unfolding. *Proc Natl Acad Sci USA* 93(18):9425–9430.
7. Frieden C, Clark AC (1997) Protein folding: How the mechanism of GroEL action is defined by kinetics. *Proc Natl Acad Sci USA* 94(11):5535–5538.
8. Chen L, Sigler PB (1999) The crystal structure of a GroEL/peptide complex: Plasticity as a basis for substrate diversity. *Cell* 99(7):757–768.
9. Buckle AM, Zahn R, Fersht AR (1997) A structural model for GroEL-polypeptide recognition. *Proc Natl Acad Sci USA* 94(8):3571–3575.
10. Landry SJ, Jordan R, McMacken R, Gierasch LM (1992) Different conformations for the same polypeptide bound to chaperones DnaK and GroEL. *Nature* 355(6359):455–457.
11. Wang Z, Feng Hp, Landry SJ, Maxwell J, Gierasch LM (1999) Basis of substrate binding by the chaperonin GroEL. *Biochemistry* 38(39):12537–12546.
12. Li Y, Gao X, Chen L (2009) GroEL recognizes an amphipathic helix and binds to the hydrophobic side. *J Biol Chem* 284(7):4324–4331.
13. Bodner CR, Dobson CM, Bax A (2009) Multiple tight phospholipid-binding modes of α-synuclein revealed by solution NMR spectroscopy. *J Mol Biol* 390(4):775–790.
14. Zahn R, Spitzfaden C, Ottiger M, Wüthrich K, Plückthun A (1994) Destabilization of the complete protein secondary structure on binding to the chaperone GroEL. *Nature* 368(6468):261–265.
15. Robinson CV, et al. (1994) Conformation of GroEL-bound α-lactalbumin probed by mass spectrometry. *Nature* 372(6507):646–651.
16. Horst R, et al. (2005) Direct NMR observation of a substrate protein bound to the chaperonin GroEL. *Proc Natl Acad Sci USA* 102(36):12748–12753.
17. Koculi E, Horst R, Horwich AL, Wüthrich K (2011) Nuclear magnetic resonance spectroscopy with the stringent substrate rhodanese bound to the single-ring variant SR1 of the *E. coli* chaperonin GroEL. *Protein Sci* 20(8):1380–1386.
18. Korzhnev DM, Kay LE (2008) Probing invisible, low-populated states of protein molecules by relaxation dispersion NMR spectroscopy: An application to protein folding. *Acc Chem Res* 41(3):442–451.
19. Skrynnikov NR, Dahlquist FW, Kay LE (2002) Reconstructing NMR spectra of "invisible" excited protein states using HSQC and HMQC experiments. *J Am Chem Soc* 124(41):12352–12360.
20. Fawzi NL, Ying J, Torchia DA, Clore GM (2010) Kinetics of amyloid β monomer-to-oligomer exchange by NMR relaxation. *J Am Chem Soc* 132(29):9948–9951.
21. Fawzi NL, Ying J, Ghirlando R, Torchia DA, Clore GM (2011) Atomic-resolution dynamics on the surface of amyloid-β protofibrils probed by solution NMR. *Nature* 480(7376):268–272.
22. Fawzi NL, Ying J, Torchia DA, Clore GM (2012) Probing exchange kinetics and atomic resolution dynamics in high-molecular-weight complexes using dark-state exchange saturation transfer NMR spectroscopy. *Nat Protoc* 7(8):1523–1533.
23. Walls KC, et al. (2012) Swedish Alzheimer mutation induces mitochondrial dysfunction mediated by HSP60 mislocalization of amyloid precursor protein (APP) and beta-amyloid. *J Biol Chem* 287(36):30317–30327.
24. Palmer AG, 3rd, Kroenke CD, Loria JP (2001) Nuclear magnetic resonance methods for quantifying microsecond-to-millisecond motions in biological macromolecules. *Methods Enzymol* 339:204–238.
25. van der Vies SM, Viitanen PV, Gatenby AA, Lorimer GH, Jaenicke R (1992) Conformational states of ribulosebisphosphate carboxylase and their interaction with chaperonin 60. *Biochemistry* 31(14):3635–3644.
26. McConnell HM (1958) Reaction rates by nuclear magnetic resonance. *J Chem Phys* 28(3):430–431.
27. Vallurupalli P, Bouvignies G, Kay LE (2011) Increasing the exchange time-scale that can be probed by CPMG relaxation dispersion NMR. *J Phys Chem B* 115(49):14891–14900.
28. Stan G, Brooks BR, Lorimer GH, Thirumalai D (2006) Residues in substrate proteins that interact with GroEL in the capture process are buried in the native state. *Proc Natl Acad Sci USA* 103(12):4433–4438.
29. Kjaergaard M, Brander S, Poulsen FM (2011) Random coil chemical shift for intrinsically disordered proteins: Effects of temperature and pH. *J Biomol NMR* 49(2):139–149.
30. Camilloni C, De Simone A, Vranken WF, Vendruscolo M (2012) Determination of secondary structure populations in disordered states of proteins using nuclear magnetic resonance chemical shifts. *Biochemistry* 51(11):2224–2231.
31. Petkova AT, et al. (2002) A structural model for Alzheimer's β-amyloid fibrils based on experimental constraints from solid state NMR. *Proc Natl Acad Sci USA* 99(26):16742–16747.
32. Scheidt HA, Morgado I, Rothemund S, Huster D, Fändrich M (2011) Solid-state NMR spectroscopic investigation of Aβ protofibrils: Implication of a β-sheet remodeling upon maturation into terminal amyloid fibrils. *Angew Chem Int Ed Engl* 50(12):2837–2840.
33. Carulla N, Zhou M, Giralt E, Robinson CV, Dobson CM (2010) Structure and intermolecular dynamics of aggregates populated during amyloid fibril formation studied by hydrogen/deuterium exchange. *Acc Chem Res* 43(8):1072–1079.
34. Elad N, et al. (2007) Topologies of a substrate protein bound to the chaperonin GroEL. *Mol Cell* 26(3):415–426.
35. Shtilerman M, Lorimer GH, Englander SW (1999) Chaperonin function: Folding by forced unfolding. *Science* 284(5415):822–825.
36. Cantor CR, Schimmel PR (1980) *The Behavior of Biological Macromolecules, Part III* (Freeman, San Francisco).
37. Todd MJ, Lorimer GH (1998) Criteria for assessing the purity and quality of GroEL. *Methods Enzymol* 290:135–141.
38. Lakomek NA, Ying JF, Bax A (2012) Measurement of ^{15}N relaxation rates in perdeuterated proteins by TROSY-based methods. *J Biomol NMR* 53(3):209–221.
39. Yip GN, Zuiderweg ER (2004) A phase cycle scheme that significantly suppresses offset-dependent artifacts in the R_2-CPMG ^{15}N relaxation experiment. *J Magn Reson* 171(1):25–36.

Supporting Information

Libich et al. 10.1073/pnas.1305715110

SI Materials and Methods

Sample Preparation. Aβ40 was prepared as described previously to produce samples >98% free of Aβ aggregates (1). Briefly, uniformly ^{15}N- or ^{13}C-labeled Aβ40, as received in the hexafluoroisopropanol-treated form from rPeptide, was dissolved in 3 mM NaOH and titrated to pH 11.0 with 50 mM NaOH [with all solutions treated with Chelex 100 (Sigma) to remove trace multivalent metal ions (2)] (final peptide concentrations of ∼400 μM), aliquoted in volumes to reconstitute 50 μM in 1 mL, flash-frozen, and lyophilized. *Escherichia coli* GroEL (3) and acid-denatured ribulose-1,5-bisphosphate carboxylase (Rubisco) (4) at natural isotopic abundance were purified as described previously and were a gift from George Lorimer and Dong Yang (University of Maryland, College Park, MD).

NMR samples were carefully prepared in matched pairs (with and without GroEL) by dissolving a single aliquot in 560 μL of Chelex 100-treated ultrapure (Milli-Q; Millipore) water, splitting the resulting mixture into two new microcentrifuge tubes, and adding 200 μL of either NMR buffer [50 mM Hepes (pH 6.3), 20% (vol/vol) D_2O, 0.02% NaN_3] or NMR buffer containing concentrated GroEL such that the final concentration of GroEL was 10, 20, or 40 μM in subunits. The GroEL stock solution was maintained in NMR buffer to ensure sample preparations resulted in a consistent pH of 6.6 and that sample-to-sample differences in pH were very small (<0.1 pH units) as judged by direct pH measurement. The chemical shifts of histidine $^1H_N/^{15}N$ cross-peaks in ^1H-^{15}N heteronuclear single quantum coherence (HSQC) correlation spectra are extremely sensitive to small changes in pH in this range and were used as an additional check for sample-to-sample consistency. Final sample conditions comprised 43 mM Hepes buffer (pH 6.6), 8% (vol/vol) D_2O, and 0.01 NaN_3, and samples were maintained at a temperature between 2 and 5 °C at all times. The matched reference samples (containing only Aβ40, without GroEL) showed no significant spectral differences, as expected.

A control sample comprising Aβ40, GroEL, and acid-denatured Rubisco was prepared to demonstrate that Aβ40 and acid-denatured Rubisco bind to the same sites on GroEL. Because acid-denatured Rubisco binds to GroEL very tightly, the presence of acid-denatured Rubisco is predicted to reduce the fraction of bound Aβ40 significantly, thereby eliminating lifetime line-broadening of Aβ40 ^{15}N resonances in the presence of GroEL. An aliquot of GroEL stock solution to yield a final concentration of 20 μM was diluted 100-fold in NMR buffer. Acid-denatured Rubisco was prepared from recombinant dimeric Rubisco dissolved in 1 mM Tris (pH 7.4) by diluting with an equal volume of 20 mM HCl (4). The acid-denatured Rubisco was slowly titrated into the diluted GroEL sample to a final concentration of 1.2-fold molar excess over GroEL binding sites (calculated as one binding site per seven GroEL monomers). The resulting mixture was concentrated using a 100-kDa molecular weight cutoff spin-filter (Amicon), diluted 100-fold, and reconcentrated (repeated three times). Rubisco binding to GroEL was assessed using Blue Native PAGE (Invitrogen) and electrospray MS (Agilent), and the resulting concentrated GroEL-Rubisco sample was used to make a 20 μM GroEL, 50 μM ^{15}N Aβ40, 2.9 μM acid-denatured Rubisco NMR sample in 43 mM Hepes (pH 6.6), 8% (vol/vol) D_2O, and 0.01% NaN_3 as described above.

NMR Spectroscopy. NMR experiments were recorded at 5 °C using Bruker Avance-III spectrometers operating at ^{1}H frequencies of 900.27 and 600.13 MHz, each equipped with Bruker TCI *z*-axis gradient cryogenic probes. Temperature differences between spectrometers were corrected by matching the chemical shift difference between residual water and 4,4-dimethyl-4-silpentane-1-sulfonate (DSS; 0 ppm) in a sample containing 43 mM Hepes (pH 6.6), 0.5% DSS, 0.01% NaN_3, and 99.9% D_2O. The set temperature on the 600-MHz spectrometer was adjusted to match the offset measured on the 900-MHz instrument. This procedure resulted in a correction of −0.3 °C (i.e., a set temperature of 4.7 °C) at 600 MHz. The ^{15}N dark-state exchange saturation transfer (DEST) experiments, differences in ^{15}N-transvere magnetization relaxation rate (R_2) values (^{15}N-ΔR_2), and ^{15}N Carr–Purcell–Meinboom–Gill (CPMG) relaxation dispersion experiments, as well as ^{15}N chemical shift differences, were measured at several combinations of external field and GroEL concentrations.

^{15}N Relaxation Measurements. ^{15}N-R_2 measurements using a relaxation-compensated CPMG scheme at 600 and 900 MHz were carried out using a ^{1}H-^{15}N HSQC-based 2D experiment exactly as described previously (5) on samples containing 50 μM ^{15}N-labeled Aβ40 in the absence and presence of 20 and 40 μM (in subunits) GroEL and in the presence of 20 μM GroEL and 2.9 μM acid-denatured Rubisco. The effective CPMG field was 550 Hz, which is sufficiently high to suppress chemical exchange-induced line-broadening completely or almost completely (Fig. S1). The ^{15}N-longitudinal magnetization relation rate (R_1) measurements for the reference Aβ40 sample (i.e., in the absence of GroEL) and with 20 μM GroEL (in monomer units) were carried out as described previously (1) (Fig. S5). In addition, ^{15}N-$R_{1\rho}$ measurements (6) were carried out at 600 and 900 MHz on samples containing 50 μM ^{15}N-labeled Aβ40 in the absence and presence of 20 μM (in subunits) GroEL.

^{15}N-DEST Spectroscopy. 2D ^{15}N-DEST experiments using the pulse sequence described previously (1) were carried out at 600 and 900 MHz on samples containing 50 μM ^{15}N-labeled Aβ40 in the presence of 20 and 40 μM GroEL. For each combination of external field and GroEL concentration, experiments were acquired as 32 interleaved spectra. Each interleaved spectrum represents a combination of the ^{15}N continuous wave (CW) saturation pulse integral to the DEST experiment applied for 0.7 s at one of 15 different offsets (21, 15, 12.5, 10, 7, 4, 2, 0, −2, −4, −7, −10, −12.5, −15, and −21 kHz at 600 MHz at both concentrations and 900 MHz at 20 μM GroEL; at 900 MHz and 40 μM GroEL, offsets used were 28, 21, 15, 10, 7, 4, 2, 0, −2, −4, −7, −10, −15, −21, and −28 kHz) from the ^{15}N carrier frequency (set at 118.5 ppm located at the center of the Aβ40 spectrum) at two rf field strengths (250 and 500 Hz), as well as two control experiments with offsets of 35 kHz and a CW field of 0 Hz. Each 2D experiment is composed of 100* × 1,260* (600 MHz) or 126* × 1,900* (900 MHz) complex points in the indirect ^{15}N and direct ^{1}H dimensions, respectively. These parameters correspond to acquisition times of 75 and 164 ms in the ^{15}N and ^{1}H dimensions, respectively, at 600 MHz, and to acquisition times of 63 and 169 ms, respectively, at 900 MHz. Experiments were acquired with 16 transients per free induction decay and an interscan delay of 1.7 s, resulting in total experiment times of about 3 d (600 MHz) and 3.5 d (900 MHz).

Processing of the 2D ^{15}N-DEST data followed that of our previous work (1). DEST profiles (i.e., ratio of cross-peak intensities as a function of CW saturation pulse frequency offset to the corresponding cross-peak intensity without saturation) were extracted from the ratio of cross-peak heights in the experiments with saturation to the average of the heights of the corresponding cross-peaks in the reference experiments without saturation. To improve the signal-to-noise ratio in the measurement of the reference intensities further, and because no measurable saturation was detected at very large offsets, data collected for absolute offsets >20 kHz were also treated as reference experiments. The fitted/predicted saturation profiles (see below) display <1% signal intensity attenuation (far less than the experimental noise) at these large offsets, further justifying this normalization procedure in an ex post fashion.

^{15}N Relaxation Dispersion. ^{15}N-CPMG (single quantum) relaxation dispersion experiments measuring ^{15}N-R_2 as a function of the CPMG field were acquired at 600 and 900 MHz for samples comprising 50 μM Aβ40 in the presence of 20 μM GroEL using a relaxation dispersion block with phase cycling designed to minimize off-resonance artifacts in the dispersion curve (7). CPMG fields, ν_{CP}, of 80, 160, 240, 320, 400, 640, 800, and 1,000 Hz, where $\nu_{\mathrm{CP}} = 1/(2\tau_{\mathrm{CP}})$ and τ_{CP} is the time between 180° ^{15}N-CPMG pulses, were applied for a constant transverse ^{15}N relaxation period of 100 ms. A reference experiment with no τ_{CP} delay was also recorded. All CPMG experiments at a given magnetic field were recorded in an interleaved manner.

^{1}H$_\mathrm{N}$ and ^{15}N Exchange-Induced Chemical Shifts. The ^{1}H$_\mathrm{N}$ and ^{15}N chemical shifts for Aβ40 at 900 MHz in the absence and presence of 10 and 20 μM GroEL were measured from a high-resolution 2D ^{1}H-^{15}N HSQC spectrum with 512* × 1,900* complex data points in the ^{15}N (indirect, F$_1$) and ^{1}H (direct, F$_2$) dimensions, respectively, corresponding to acquisition times of 225 and 169 ms, respectively. Time domain data in the ^{15}N and ^{1}H dimensions were apodized with a 90°-shifted sine function and zero-filled to yield a 4,096* × 4,096* data matrix with digital resolutions of 0.56 and 2.6 Hz, respectively. It is important to note that absolute chemical shifts are sensitive in the 1-Hz range to small, otherwise undetectable, sample-to-sample differences (e.g., pH, salt concentration); therefore, a reference sample prepared in parallel from the same lyophilized Aβ40 aliquot was used as the chemical shift reference for each condition (i.e., the Aβ40 samples with 10 and 20 μM GroEL each had a distinct reference sample) to permit measurement of exchange-induced shifts to an accuracy of better than 0.1 Hz. The accuracy of this protocol is evident from the excellent correlation between the exchange-induced shifts measured in the presence of 10 and 20 μM GroEL (Fig. 2*D*). Chemical shifts in each spectrum were extracted by automated peak picking in NMRPipe (8) using a customized script in which the interpolation region was set to be approximately half of the average line width (taken over all peaks) and the detection region was set to half of the value used for the interpolation region. Errors in the peak positions due to random noise were determined using NMRPipe as described (9).

^{13}C Exchange-Induced Chemical Shifts. ^{13}Cα and ^{13}Cβ chemical shift changes on addition of GroEL were measured from ^{1}H-^{13}C constant time (CT)-HSQC spectra (10, 11). To achieve the necessary high resolution to permit accurate determination of small ^{13}C chemical shift differences, a 56-ms CT delay was used for the CT-HSQC experiments, permitting the one-bond ^{13}C-^{13}C J coupling ($^1J_{\mathrm{CC}}$) coupling of the aliphatic side chains to evolve for two full cycles, and thereby to be effectively removed. A gradient-enhanced detection scheme (12) was used, which not only yields higher sensitivity but facilitates solvent suppression by application of the decoding gradient pulse before ^{1}H detection in the acquisition dimension. To suppress the solvent signal further, a very weak presaturation pulse with an rf field strength of ∼31 Hz was applied on resonance with the water peak during the interscan delay of 1 s. Although saturation transfer from water to exchangeable protons (e.g., amide, side-chain hydroxyl groups), followed by spin diffusion to aliphatic protons, may potentially reduce the sensitivity of ^{13}C-^{1}H CT-HSQC spectra, we found this effect was negligible in the case of the essentially unstructured Aβ40. The ^{1}H-^{13}C CT-HSQC spectra were acquired with 594* × 1,900* complex data points and acquisition times of 54.7 and 145 ms in the ^{13}C (indirect) and ^{1}H (direct) dimensions, respectively. Time domain data were apodized with a 90°-shifted sine function and zero-filled, resulting in a 4,096* × 4,096* complex data matrix with digital resolutions of 2.4 and 3.0 Hz in the ^{13}C and ^{1}H dimensions, respectively. Chemical shifts in each spectrum were measured and extracted as described for ^{15}N shifts; however, in addition, because the ^{13}C exchange-induced shifts are very small, the measurements were repeated three times each in the presence and absence of GroEL.

^{13}C-R_2 Measurements on Free Aβ40. For the determination of ^{13}C-R_2, ^{13}C-$R_{1\rho}$ and ^{13}C-R_1 measurements were carried out using the same basic CT-HSQC pulse scheme as used for measuring exchange-induced ^{13}C chemical shifts (see above) but were extended for ^{13}C relaxation measurements by incorporation of suitable blocks. Similar to ^{15}N relaxation (6) and methyl ^{13}C-$R_{1\rho}$ (13) relaxation measurements, additional pulse sequence segments were incorporated into the basic CT-HSQC scheme for rephasing $2C_zH_z$ magnetization into C_z after the initial insensitive nuclei enhanced by polarization transfer (INEPT), performing a spin lock in the case of $R_{1\rho}$ or allowing a variable delay for R_1 measurements, and dephasing back to antiphase magnetization during the CT t_1 before gradient-enhanced detection. ^{13}Cα and ^{13}Cβ $R_{1\rho}$ rates were measured with separate experiments by setting the carrier to 58 ppm and 35.8 ppm for Cα and Cβ, respectively. $R_{1\rho}$ spectra were recorded in an interleaved fashion with variable spin-lock periods of 3, 12, 25, 50, and 113 ms at 3.8 kHz (900 MHz) or at 3, 8, 20, 50, 90, and 150 ms at 2.8 kHz (600 MHz), whereas R_1 experiments used delays of 0, 80, 240, 400, 480, and 640 ms. Note that for methylene CH$_2$ groups, refocusing into a pure C_z term at the end of the rephasing INEPT is difficult due to the presence of a $4C_zH^1_zH^2_z$ term that cannot be completely eliminated by a simple proton purge pulse. In addition, unlike the case for the Cα of nonglycine residues, the ^{13}C magnetization of CH$_2$ groups is expected to decay nonexponentially, largely as a result of ^{1}H-^{13}C dipole-dipole cross-correlated relaxation. The same is true of alanine methyl groups, where multiexponential behavior is expected owing to different decay rates for the 1/2 and 3/2 manifolds. Although these caveats complicate the measurement of methyl and methylene ^{13}C relaxation rates needed for precise probing of the dynamics of these groups, the resulting apparent ^{13}C-R_2 rates are sufficient to establish the approximate ratio of ^{13}Cα to ^{13}Cβ R_2 values within a given residue of free Aβ40. The ^{13}C-R_2 values were calculated from ^{13}C-$R_{1\rho}$ and ^{13}C-R_1 values using the equation:

$$R_2 = \left[R_{1\rho} - R_1\cos^2(\theta)\right]/\sin^2(\theta), \qquad \textbf{[S1]}$$

where θ is the angle between the effective spin-lock field and the external magnetic field (where 90° represents a resonance exactly on-resonance with the spin-lock field). The ratio of ^{13}Cβ to ^{13}Cα R_2 values was found to be ∼0.9 with the exception of alanine methyl groups, in which the apparent ratio was about 0.5.

Simultaneous Fitting of ^{15}N DEST, ΔR_2, Relaxation Dispersion, and Observed Chemical Shift Deviations to a Two-State Kinetic Model. The experimental ^{15}N-DEST profiles (eight datasets from two samples containing 50 μM Aβ40 in the presence of 20 and 40 μM GroEL recorded at spectrometer frequencies of 600 and 900 MHz with CW rf field strengths of 250 and 500 Hz), ^{15}N-ΔR_2 values (four datasets comprising the same two samples at 600 and 900 MHz vs. the matched samples in the absence of GroEL), ^{15}N relaxation dispersion (two datasets at 600 and 900 MHz using the sample containing 20 μM GroEL), and ^{15}N chemical shift differences between the Aβ40 samples in the absence and presence of 20 μM GroEL (two datasets at 600 and 900 MHz) were used together to perform a single simultaneous fit to a two-state model (Fig. 3) optimizing two global parameters, $k_{\mathrm{on}}^{\mathrm{app}}$ and the fraction p_{A} of free Aβ40, and two sets of residue-specific parameters, the $^{15}\mathrm{N}\text{-}R_{2,\mathrm{calc}}^{\mathrm{GroEL\text{-}bound}}(i)$ values for GroEL-bound Aβ40 and the ^{15}N chemical shift differences $\Delta\omega_{\mathrm{N}}(i)$ between GroEL-bound and free Aβ40. [Note the fraction p_{B} of GroEL-bound Aβ40 is given by $1 - p_{\mathrm{A}}$ and the dissociation constant k_{off} is given by $k_{\mathrm{on}}^{\mathrm{app}} p_{\mathrm{A}}/(1 - p_{\mathrm{A}})$]. The four different experiments for all measured residues determine the optimized values of $k_{\mathrm{on}}^{\mathrm{app}}$ and p_{A}. The four different experiments for any given residue i determine the optimized value of that residue's $^{15}\mathrm{N}\text{-}R_{2,\mathrm{calc}}^{\mathrm{GroEL\text{-}bound}}(i)$, and the ^{15}N relaxation dispersion and exchange-induced ^{15}N-shift data for any given residue i determine the optimized value of that residue's $\Delta\omega_{\mathrm{N}}(i)$.

As we described previously (1, 5), the time-dependent magnetization in both DEST and ΔR_2 experiments can be represented by a homogeneous form of the McConnell equations (14, 15). For a single isolated spin in two-site exchange:

$$\frac{\mathrm{d}}{\mathrm{d}t}\begin{bmatrix} E/2 \\ I_x^{\mathrm{A}} \\ I_y^{\mathrm{A}} \\ I_z^{\mathrm{A}} \\ I_x^{\mathrm{B}} \\ I_y^{\mathrm{B}} \\ I_z^{\mathrm{B}} \end{bmatrix} = \begin{bmatrix} 0 & 0 & 0 & 0 & 0 & 0 & 0 \\ 0 & R_2^{\mathrm{A},0} + k_{\mathrm{on}}^{\mathrm{app}} & \Omega^{\mathrm{A}} & -\omega_y & -k_{\mathrm{off}} & 0 & 0 \\ 0 & -\Omega^{\mathrm{A}} & R_2^{\mathrm{A},0} + k_{\mathrm{on}}^{\mathrm{app}} & \omega_x & 0 & -k_{\mathrm{off}} & 0 \\ -2\Theta^{\mathrm{A}} & \omega_y & -\omega_x & R_1^{\mathrm{A}} + k_{\mathrm{on}}^{\mathrm{app}} & 0 & 0 & -k_{\mathrm{off}} \\ 0 & -k_{\mathrm{on}}^{\mathrm{app}} & 0 & 0 & R_2^{\mathrm{B},0} + k_{\mathrm{off}} & \Omega^{\mathrm{B}} & -\omega_y \\ 0 & 0 & -k_{\mathrm{on}}^{\mathrm{app}} & 0 & -\Omega^{\mathrm{B}} & R_2^{\mathrm{B},0} + k_{\mathrm{off}} & \omega_x \\ -2\Theta^{\mathrm{B}} & 0 & 0 & -k_{\mathrm{on}}^{\mathrm{app}} & \omega_y & -\omega_x & R_1^{\mathrm{B}} + k_{\mathrm{off}} \end{bmatrix} \times \begin{bmatrix} E/2 \\ I_x^{\mathrm{A}} \\ I_y^{\mathrm{A}} \\ I_z^{\mathrm{A}} \\ I_x^{\mathrm{B}} \\ I_y^{\mathrm{B}} \\ I_z^{\mathrm{B}} \end{bmatrix}, \qquad \textbf{[S2]}$$

where I represents the rotating frame magnetization of a ^{15}N nucleus in the free and GroEL-bound states (denoted by the superscripts A and B, respectively). R_1 and R_2 are the longitudinal and transverse magnetization relaxation rates (where the additional superscript 0 for R_2 signifies the transverse relaxation rate in the absence of exchange between states A and B); Ω is the difference between the peak resonant frequency and the frequency of the applied saturation field; ω is the strength of the CW saturation field (0 for ΔR_2 experiments) about the given axis (x or y); E is unity; and $\Theta^n = R_1^n I_{z,0}^n$, where $I_{z,0}^n$ is the equilibrium longitudinal magnetization of state n. The initial magnetization is entirely longitudinal (i.e., only the I_z terms are nonzero) for the DEST experiment and transverse (i.e., only the I_x terms are nonzero) for the ΔR_2 experiment (1).

The DEST experimental observable κ, the ratio of the signal intensity of the resonance as a function of saturation offset and saturation field to that without saturation, can be calculated as described previously (1, 16). Briefly, the numerical solution for I_z^{A} after the CW saturation time of 0.7 s at each combination of saturation offset Ω, saturation field ω_x, residue position, external field condition (900 and 600 MHz), and concentration of GroEL (20 and 40 μM) was calculated as a function of saturation offset by solving Eq. **S2** using the matrix exponential function in the program MATLAB (MathWorks). The value of κ was computed by calculating I_z^{A} for both initial ^{15}N magnetization conditions during the saturation period (on the $+z$ and $-z$ axes, I_{+z} and I_{-z}); the difference, $I_{+z} - I_{-z}$, is then computed and finally normalized to the solution without saturation. $R_2^{\mathrm{A},0}$, R_1^{A} (Fig. S5), and Ω^{A} for each residue were set to the experimental values measured in the absence of GroEL, and R_1^B for Aβ40 in the dark state bound to GroEL was set to an estimated constant value of 0.5 s^{-1}, the value of which we have previously shown does not affect the results by design of the experiment (1). The value of $k_{\mathrm{on}}^{\mathrm{app}}$ in the presence of 40 μM GroEL was assumed to be twice as high as that in the presence of 20 μM GroEL, an assumption that is perfectly reasonable because the observed values of ΔR_2 are linearly proportional to the concentration of GroEL over a range of 10–40 μM in subunits (Fig. S2 *C* and *D*), reflecting the linear dependence of $^{15}\mathrm{N}\text{-}\Delta R_2$ on the pseudo-first order association rate constant, $k_{\mathrm{on}}^{\mathrm{app}}$, given by $k_{\mathrm{on}}^{\mathrm{app}} = k_{\mathrm{on}}[\mathrm{GroEL}]_{\mathrm{free}} \approx k_{\mathrm{on}}[\mathrm{GroEL}]_{\mathrm{total}}/([\mathrm{A}\beta40]_{\mathrm{total}} K_{\mathrm{A}} + 1)$, where k_{on} is the second order association rate constant and K_{A} is the equilibrium association constant. For the purposes of fitting the ^{15}N-DEST data, one can readily assume that the ^{15}N chemical shifts in the visible and dark states are equal ($\Omega^{\mathrm{A}} = \Omega^{\mathrm{B}}$), since any shift differences are very small compared with the width of the DEST saturation profiles (16). However, in this instance, the chemical shifts in the bound state are afforded from fitting the ^{15}N relaxation dispersion and exchange-induced ^{15}N shift data (see below), allowing the Ω^{B} values to be obtained explicitly.

ΔR_2 was calculated by propagating Eq. **S2** with initial magnetization only on the transverse (e.g., x) axis using a simple two-time point single exponential decay for computing the effective $^{15}\mathrm{N}\text{-}R_2$:

$$\Delta R_2 = \frac{ln\left[I_x^{\mathrm{A}}(\tau_1)/I_x^{\mathrm{A}}(\tau_2)\right]}{\tau_2 - \tau_1} - R_2^{\mathrm{A},0}, \qquad \textbf{[S3]}$$

where the delays τ_1 and τ_2 were set to 10 and 30 ms, respectively; τ_1 was chosen to remove any small deviations from exponential behavior at very short delays, and τ_2 was chosen to match the order of magnitude of the experimental delays used to measure R_2 in the case of fast relaxation ($R_2 \sim 25$ s^{-1}). For the fitting of ΔR_2, states A and B were assumed, for ease of implementation, to have the same chemical shift, because relaxation enhancement arising from chemical exchange is virtually completely suppressed in the experimental $^{15}\mathrm{N}\text{-}R_2$ measurements, which incorporate a 550-Hz CPMG train (i.e., the increase in $^{15}\mathrm{N}\text{-}R_2$ values for Aβ40 in the presence of GroEL is almost entirely due to lifetime broadening arising from the higher intrinsic $^{15}\mathrm{N}\text{-}R_2$ values of the dark GroEL-bound state). For Aβ40 in the absence of GroEL, no measurable ^{15}N relaxation dispersion is observed for any residue; in the presence of GroEL, a few residues of Aβ40 show a very small amount of ^{15}N relaxation dispersion in CPMG experiments, which entail very small corrections in the observed ΔR_2 values (the largest of which is less than 0.5 s^{-1} in the presence of 20 μM GroEL at a spectrometer frequency of 900 MHz and a CPMG field of 550 Hz; Fig. S1). To completely remove any contribution to ΔR_2 from residual chemical exchange effects at a CPMG field of 550 Hz, experimental ΔR_2 values at each residue and B_0 field were corrected by simply subtracting any residual intermediate chemical exchange contributions still present at 550 Hz [estimated by R_2(550 Hz) − R_2(5,000 Hz) for the previous fit iteration of the relaxation dispersion curves; see below].

For the ^{15}N-CPMG experiments, an analytical expression for the apparent $R_2(R_2^{\text{app},\ 1/(2\tau_{\text{CP}})})$ of the resonances of free Aβ40 as a function of CPMG field ($1/2\tau_{\text{CP}}$), valid in all exchange and population regimes, was used (17):

$$R_2^{\text{app},1/(2\tau_{\text{CP}})} = \frac{1}{2}\left(R_2^{\text{A},0} + R_2^{\text{B},0} + k_{\text{ex}} - \frac{1}{\tau_{\text{CP}}}\cosh^{-1}[D_+\cosh(\eta_+) - D_-\cos(\eta_-)]\right), \qquad \textbf{[S4]}$$

where τ_{CP} is the delay between 180° pulses in the CPMG pulse train:

$$\begin{aligned} D_\pm &= \frac{1}{2}\left[\frac{\Psi + 2\cdot\Delta\omega_{\text{N}}^2}{\left(\Psi^2+\zeta^2\right)^{1/2}} \pm 1\right] \\ \eta_\pm &= \frac{\tau_{\text{CP}}}{\sqrt{2}}\left[\left(\Psi^2+\zeta^2\right)^{1/2} \pm \Psi\right]^{1/2} \\ \Psi &= \left[R_2^{\text{A},0} - R_2^{\text{B},0} - k_{\text{ex}}(p_{\text{A}} - p_{\text{B}})\right]^2 - \Delta\omega_{\text{N}}^2 + 4p_{\text{A}}p_{\text{B}}(k_{\text{ex}})^2 \\ \zeta &= 2\cdot\Delta\omega_{\text{N}}\left[R_2^{\text{A},0} - R_2^{\text{B},0} - k_{\text{ex}}(p_{\text{A}} - p_{\text{B}})\right], \end{aligned} \qquad \textbf{[S5]}$$

and $\Delta\omega_{\text{N}}$ is the chemical shift difference (in units of rad·s^{-1}) between the free and GroEL-bound states of Aβ40, $k_{\text{ex}}(=k_{\text{on}}^{\text{app}} + k_{\text{off}})$ is the overall exchange rate, and p_{A} and p_{B} (= 1 − p_A) are the fractions of free and GroEL-bound Aβ40, respectively.

The exchange-induced ^{15}N shifts ($\delta_{\text{N}}^{\text{ex}}$ in units of hertz) observed for Aβ40 in the presence of GroEL were calculated using (18)

$$\delta_{\text{N}}^{\text{ex}} = \frac{k_{\text{on}}^{\text{app}} k_{\text{off}} \Delta\omega_{\text{N}}/2\pi}{\left(k_{\text{off}} + R_2^{\text{B},0} - R_2^{\text{A},0}\right)^2 + \Delta\omega_{\text{N}}^2}, \qquad \textbf{[S6]}$$

where $\Delta\omega_{\text{N}}/2\pi$ is the difference in ^{15}N chemical shifts (^{15}N-Δδ) in units of hertz between the free and GroEL-bound states.

All the experimental data were fit simultaneously by minimizing the sum of the squared difference, F, between the observed and calculated values of the experimental observables using a custom MATLAB program implementing Eqs. **S2**–**S6**:

$$\begin{aligned} F = {} & \alpha_1 \sum_i \sum_{l=1}^{2} \sum_{m=1}^{2} \left(\frac{\Delta R_2^{\text{obs},i,l,m} - \Delta R_2^{\text{calc},i,l,m}}{\sigma_{\Delta R_2^{\text{obs},i,l,m}}}\right)^2 + \alpha_2 \sum_i \sum_j \sum_{k=1}^{2} \sum_{l=1}^{2} \sum_{m=1}^{2} \left(\kappa^{\text{obs},i,j,k,l,m} - \kappa^{\text{calc},i,j,k,l,m}\right)^2 \\ & + \alpha_3 \sum_i \sum_n \sum_{m=1}^{2} \left(\frac{R_2^{\text{app,obs},i,n,m} - R_2^{\text{app,calc},i,n,m}}{\sigma_{R_2^{app,obs,i,n,m}}}\right)^2 + \alpha_4 \sum_i \sum_{m=1}^{2} \left(\delta_{\text{N}}^{\text{ex,obs},i} - \delta_{\text{N}}^{\text{ex,calc},i}\right)^2, \end{aligned} \qquad \textbf{[S7]}$$

where the subscripts i, j, k, l, m, and n refer to residue number, DEST offset, DEST field strength (250 and 500 Hz), GroEL concentration (20 and 40 μM), ^{1}H spectrometer frequency (600 and 900 Hz), and CPMG field, respectively, and α_1, α_2, α_3, and α_4 represent empirically determined constants used to weight the different data types appropriately and have numerical values of 0.1, 1, 10, and 500, respectively. Note that because the uncertainties in the measured values of ΔR_2 and the relaxation dispersion ($R_2^{\text{app},1/(2\tau_{\text{CP}})}$) data vary significantly, the differences between observed and predicted values were divided by the uncertainties in the observed values. The uncertainties in the values of the optimized parameters, corresponding to confidence intervals of ±1 SD, were determined from the nonlinear fit Jacobian matrix using the MATLAB function *nlparci*. Convergence of the solution was confirmed by varying initial values for all parameters and obtaining the same solution within reported uncertainties. Because there are only two global parameters ($k_{\text{on}}^{\text{app}}$ and p_{A}) with the remaining parameters, ^{15}N-$R_{2,\text{calc}}^{\text{GroEL-bound}}(i)$ and $\Delta\omega_{\text{N}}(i)$, entirely local to each residue position, the range of possible solutions in multidimensional parameter space is easily sampled.

It is important to note that the four experiments are influenced in different ways by the interplay of the exchange rates and residue-specific ^{15}N-$R_{2,\text{calc}}^{\text{GroEL-bound}}(i)$ and, as a result, are highly complementary to one another. For example, the ΔR_2 measurements place a lower limit on the value of $k_{\text{on}}^{\text{app}}$ because the extent of lifetime line-broadening cannot exceed the value of $k_{\text{on}}^{\text{app}}$, and the value of $\Delta R_2(i)$ is only influenced by the values of k_{off} and ^{15}N-$R_{2,\text{calc}}^{\text{GroEL-bound}}(i)$ when the magnitude of k_{off} is comparable to or larger than ^{15}N-$R_{2,\text{calc}}^{\text{GroEL-bound}}(i)$ (as is the case here). When $k_{\text{off}} \ll {}^{15}\text{N-}R_{2,\text{calc}}^{\text{GroEL-bound}}(i)$, $\Delta R_2 = k_{\text{on}}^{\text{app}}$. The ^{15}N-DEST profiles are sensitive to the values of both k_{off} and $k_{\text{on}}^{\text{app}}$, as well as to the values of ^{15}N-$R_{2,\text{calc}}^{\text{GroEL-bound}}(i)$ of course, but they are effectively independent of the chemical shift differences $\Delta\omega_{\text{N}}(i)$ between free and bound Aβ40 (as are the values of ΔR_2). Both the relaxation dispersion curves and exchange-induced shifts are dependent on the chemical shift differences $\Delta\omega_{\text{N}}(i)$ between free and bound Aβ40; however, whereas the exchange-induced shift values (which can be measured very accurately) are directly dependent on $\Delta\omega_{\text{N}}(i)$, $\Delta\omega_{\text{N}}(i)$ values modulate both the amplitude and shape of the dispersion curves. The exchange-induced shifts, however, are only dependent on ^{15}N-$R_{2,\text{calc}}^{\text{GroEL-bound}}(i)$ when ^{15}N-$R_{2,\text{calc}}^{\text{GroEL-bound}}(i)$ is of the same order of magnitude or larger than k_{off} (as is the case here). When $k_{\text{off}} \gg {}^{15}\text{N-}R_{2,\text{calc}}^{\text{GroEL-bound}}(i)$, the exchange-induced shift is independent of ^{15}N-$R_{2,\text{calc}}^{\text{GroEL-bound}}(i)$.

It is worth noting that for the current system, the relaxation dispersion data alone are insufficient to determine the exchange rates precisely because the small magnitude of the observed dispersions (Fig. 1*D*) and the concomitant experimental uncertainties result in a shallow minimum with reasonably acceptable fits for quite a broad range of kinetic parameters. For example, when the experimental ^{15}N exchange-induced shifts ($\delta_{\text{N}}^{\text{ex}}$) are omitted from the global optimization, the relaxation dispersion, DEST, and ΔR_2 data can be equally well fit with a $k_{\text{on}}^{\text{app}}$ value as low as 15 s^{-1} (and k_{off} = 1,180 s^{-1}) but the calculated $\delta_{\text{N,calc}}^{\text{ex}}$values are underpredicted (the maximum value of $|\delta_{\text{N,calc}}^{\text{ex}}|$ is 0.9 Hz compared with an observed value of 1.3 Hz, and many $\delta_{\text{N,calc}}^{\text{ex}}$ values are zero because there is no measurable dispersion at many residues) and the maximum value of $^{15}\mathrm{N}$-$R_{2,\mathrm{calc}}^{\mathrm{GroEL\text{-}bound}}$ is ~2,500 s^{-1}, a factor of 2.5 larger than expected for a system of this size. If only the relaxation dispersion data for the 12 residues (F4, R5, V18, F19, F20, A21, K28, G33, M35, V36, V39, and V40) that show any significant dispersion are used in the minimization, a reasonable fit can be obtained with $k_{\mathrm{on}}^{\mathrm{app}} = 162\ \mathrm{s}^{-1}$ and $k_{\mathrm{off}} = 6{,}040\ \mathrm{s}^{-1}$; however, the $\delta_{\mathrm{N,calc}}^{\mathrm{ex}}$ values are far too large with a maximum value of 23 Hz and the maximum $^{15}\mathrm{N}$-$R_{2,\mathrm{calc}}^{\mathrm{GroEL\text{-}bound}}$ value (240 s^{-1}) is too small. Inclusion of the exchange-induced chemical shifts was therefore critical for accurate determination of the exchange rate constants and further provided chemical shift information at almost every residue position. Thus, analysis of exchange-induced chemical shifts, which are readily measured from a pair of 2D heteronuclear correlation spectra, represents a generally applicable approach for quantitative analysis of chemical exchange in interacting systems that display small relaxation dispersion effects either because the exchange regime lies close to or outside the range that can be probed by relaxation dispersion or because the chemical shift differences between the major and minor states are small.

Conversely, it is also important to note that the relaxation dispersion data, although insufficient to define the values of the global exchange parameters uniquely in the absence of the observed exchange-induced chemical shifts, are also dependent on the chemical shift differences between free and bound Aβ40, and provide critical restraints on the fit. When the relaxation dispersion data are omitted, global kinetic and local chemical shift parameters that result in reasonably good fits to the other experimental data within experimental error can be found. However, the solutions obtained on exclusion of the relaxation dispersion data are not unique. Although solutions can be found that fit the data adequately with values of the various optimized parameters that differ quite significantly (i.e., outside the ±1 SD confidence intervals) from those obtained when the relaxation dispersion data are included in the global fitting, these solutions do not predict the observed relaxation dispersion curves correctly. Although the solutions found by including the relaxation dispersion data are among the possible solutions of course, the potential solutions found when the relaxation dispersion data are excluded span a large range of parameters, predicting anything from large relaxation dispersions that are clearly not observed in the experimental data to very little dispersion at all sites. Thus, inclusion of the relaxation dispersion data in the global fitting is also critical.

As noted above, only 12 residues show significant relaxation dispersion above experimental noise and artifacts. In the global fitting, however, we included the relaxation dispersion data for all residues. Although not strictly required, the latter are useful because they place stringent upper limits on the chemical shift differences between the free and bound states for residues that do not exhibit any measurable relaxation dispersion.

$^{15}\mathrm{N}$-R_2 Rates Measured by Relaxation-Compensated CPMG vs. $R_{1\rho}$.

Both relaxation-compensated CPMG (19) and $R_{1\rho}$ (6) were used for the measurement of $^{15}\mathrm{N}$-R_2 rates. The $R_{1\rho}$ experiment (corrected for off-resonance effects; see Eq. **S1**) measures the R_2 rate of in-phase N_x coherence; the relaxation-compensated CPMG experiment, on the other hand, measures the average relaxation rate of antiphase $2\mathrm{N}_y\mathrm{H}_z$ and in-phase N_x coherences. Although the difference between the relaxation rates of $2\mathrm{N}_y\mathrm{H}_z$ and N_x for an isolated $^{15}\mathrm{N}$-$^{1}\mathrm{H}$ spin system is negligibly small, for a protonated polypeptide, the antiphase term relaxes faster than the in-phase coherence by a term R_{ext} (also known as scalar relaxation of the second kind) given by:

$$R_{\mathrm{ext}} = \rho_{\mathrm{HH}} + k_{\mathrm{ex}}^{\mathrm{water}}, \qquad \textbf{[S8]}$$

where ρ_{HH} is the sum of the amide $^{1}\mathrm{H}$ relaxation rates as a result of dipolar interaction of the backbone amide proton with all other nearby protons in space and $k_{\mathrm{ex}}^{\mathrm{water}}$ is the water exchange rate. The relaxation-compensated CPMG R_2 therefore contains an additional $R_{\mathrm{ext}}/2$ term relative to the pure in-phase R_2 ($R_2^{\mathrm{in\text{-}phase}}$) measured in the $R_{1\rho}$ experiment:

$$R_2^{\mathrm{CPMG}} = R_2^{\mathrm{in\text{-}phase}} + R_{\mathrm{ext}}/2. \qquad \textbf{[S9]}$$

Under the experimental conditions used (pH 6.5 at 5 °C), the contribution from solvent exchange ($k_{\mathrm{ex}}^{\mathrm{water}}$) is small even for an unstructured peptide. Moreover, the $k_{\mathrm{ex}}^{\mathrm{water}}$ contribution is canceled out forΔR_2, because this rate is expected to be the same in the free and bound states. The ρ_{HH}, however, can make a significant contribution to the value of the relaxation-compensated CPMG R_2 (R_2^{CPMG}) in the GroEL-bound state, because ρ_{HH} is proportional to the effective correlation time (on a residue basis), and therefore to $R_2^{\mathrm{in\text{-}phase}}$. Thus, as expected, $\Delta R_2^{\mathrm{CPMG}}$ and $\Delta R_2^{\mathrm{in\text{-}phase}}$ are highly correlated with a slope of 1.11 at 900 MHz (Fig. S6*A*). Similarly, $R_2^{\mathrm{CPMG,bound}}$ and $R_2^{\mathrm{in\text{-}phase,bound}}$, calculated by least-squares optimization (see Eqs. **S2** and **S3**) from the experimental 900-MHz R_2^{CPMG} and $R_2^{\mathrm{in\text{-}phase}}$ data, respectively, measured in the presence and absence of GroEL, with the kinetic rate constants set to the values determined independently from the CPMG relaxation dispersion curves and exchange-induced shift data, are highly correlated with a slope of 1.12 at 900 MHz (Fig. S6*B*). Because ρ_{HH} is field-independent in the spin-diffusion limit, the slope of $R_2^{\mathrm{CPMG,bound}}$ vs. $R_2^{\mathrm{in\text{-}phase,bound}}$ will increase at a lower magnetic field: At 600 MHz, that slope is calculated to be 1.15.

Both $^{15}\mathrm{N}$-R_2 of free Aβ40 and $^{15}\mathrm{N}$-ΔR_2 are used in the joint fits to the DEST, ΔR_2, CPMG relaxation dispersion, and exchange-induced chemical shift data. The question then arises about which R_2 should be used in fitting the different types of data.

The computation of ΔR_2, as formulated by Eqs. **S2** and **S3**, formally uses the ratio of in-phase magnetization at times τ_1 and τ_2, and is therefore directly applicable to the analysis of $\Delta R_2^{\mathrm{in\text{-}phase}}$ measured from the $R_{1\rho}$ experiments. However, the same formulation is equally applicable to $\Delta R_2^{\mathrm{CPMG}}$ obtained using the relaxation-compensated CPMG experiment by simply replacing the $R_2^{\mathrm{in\text{-}phase}}$ terms in Eq. **S2** by R_2^{CPMG}. The experimental ΔR_2 data used in the global fitting presented in the main text and shown in the figures of the main text relate to $\Delta R_2^{\mathrm{CPMG}}$. This was done to simplify the calculations, because R_2^{CPMG} is naturally the appropriate R_2 for the analysis of the relaxation-compensated CPMG relaxation dispersion data, as well as the exchange-induced chemical shifts (see below).

The $^{1}\mathrm{H}_{\mathrm{N}}$ and $^{15}\mathrm{N}$ exchange-induced chemical shifts were measured from HSQC experiments in which the one-bond N-H J coupling ($^{1}J_{\mathrm{NH}}$) Hamiltonian evolves for $t_1/2$, although the overall evolution is refocused by a 180° proton pulse in the middle of t_1. This results in the presence of both in-phase and antiphase magnetization for an approximately equal amount of time, on average. Therefore, R_2^{CPMG} is the relevant R_2 for fitting the exchange-induced chemical shifts using Eq. **S6**. The same is true for the $^{13}\mathrm{C}$ exchange-induced shifts from a CT-HSQC experiment.

In the DEST experiment (see the pulse scheme shown in figure S8 of ref. 1), the $^{15}\mathrm{N}$ saturation pulse is applied to in-phase N_z magnetization, and Eq. **S2** only includes in-phase transverse coherence terms in both free and bound states. Thus, in principle, the $R_2^{\mathrm{in\text{-}phase}}$ values obtained from an $R_{1\rho}$ experiment should be used for fitting the DEST data. However, it should be noted that the in-phase transverse magnetization created during the DEST saturation could potentially evolve into a small amount of antiphase coherence. To evaluate how the use of only the in-phase basis coherences in Eq. **S2** may affect the accuracy of the DEST effect, the attenuation of the observable I_z^{A} intensity was simulated using both Eq. **S2** and the expanded equation below, which includes both in-phase and antiphase coherences:

$$\frac{d}{dt}\begin{bmatrix} E/2 \\ I_x^{\mathrm{A}} \\ I_y^{\mathrm{A}} \\ I_z^{\mathrm{A}} \\ I_x^{\mathrm{B}} \\ I_y^{\mathrm{B}} \\ I_z^{\mathrm{B}} \\ 2I_x^{\mathrm{A}}H_z^{\mathrm{A}} \\ 2I_y^{\mathrm{A}}H_z^{\mathrm{A}} \\ 2I_z^{\mathrm{A}}H_z^{\mathrm{A}} \\ 2I_x^{\mathrm{B}}H_z^{\mathrm{B}} \\ 2I_y^{\mathrm{B}}H_z^{\mathrm{B}} \\ 2I_z^{\mathrm{B}}H_z^{\mathrm{B}} \end{bmatrix} =$$

$$-\begin{bmatrix}
0 & 0 & 0 & 0 & 0 & 0 & 0 & 0 & 0 & 0 & 0 & 0 & 0 \\
0 & R_2^{\mathrm{A,0,in\text{-}phase}}+k_{\mathrm{on}}^{\mathrm{app}} & \Omega^{\mathrm{A}} & -\omega_y & -k_{\mathrm{off}} & 0 & 0 & \eta_{xy}^{\mathrm{A}} & \pi J & 0 & 0 & 0 & 0 \\
0 & -\Omega^{\mathrm{A}} & R_2^{\mathrm{A,0,in\text{-}phase}}+k_{\mathrm{on}}^{\mathrm{app}} & \omega_x & 0 & -k_{\mathrm{off}} & 0 & -\pi J & \eta_{xy}^{\mathrm{A}} & 0 & 0 & 0 & 0 \\
-2\Theta^{\mathrm{A}} & \omega_y & -\omega_x & R_1^{\mathrm{A}}+k_{\mathrm{on}}^{\mathrm{app}} & 0 & 0 & -k_{\mathrm{off}} & 0 & 0 & \eta_z^{\mathrm{A}} & 0 & 0 & 0 \\
0 & -k_{\mathrm{on}}^{\mathrm{app}} & 0 & 0 & R_2^{\mathrm{B,0,in\text{-}phase}}+k_{\mathrm{off}} & \Omega^{\mathrm{B}} & -\omega_y & 0 & 0 & 0 & \eta_{xy}^{\mathrm{B}} & \pi J & 0 \\
0 & 0 & -k_{\mathrm{on}}^{\mathrm{app}} & 0 & -\Omega^{B} & R_2^{\mathrm{B,0,in\text{-}phase}}+k_{\mathrm{off}} & \omega_x & 0 & 0 & 0 & -\pi J & \eta_{xy}^{\mathrm{B}} & 0 \\
-2\Theta^{\mathrm{B}} & 0 & 0 & -k_{\mathrm{on}}^{\mathrm{app}} & \omega_y & -\omega_x & R_1^{\mathrm{B}}+k_{\mathrm{off}} & 0 & 0 & 0 & 0 & 0 & \eta_z^{\mathrm{B}} \\
0 & \eta_{xy}^{\mathrm{A}} & \pi J & 0 & 0 & 0 & 0 & R_2^{\mathrm{A},1} & \Omega^{\mathrm{A}} & -\omega_y & -k_{\mathrm{off}} & 0 & 0 \\
0 & -\pi J & \eta_{xy}^{\mathrm{A}} & 0 & 0 & 0 & 0 & -\Omega^{\mathrm{A}} & R_2^{\mathrm{A},1} & \omega_x & 0 & -k_{\mathrm{off}} & 0 \\
0 & 0 & 0 & \eta_z^{\mathrm{A}} & 0 & 0 & 0 & \omega_y & -\omega_x & R_1^{\mathrm{A}}+\rho_{\mathrm{HH}}^{\mathrm{A}}+k_{\mathrm{on}}^{\mathrm{app}} & 0 & 0 & -k_{\mathrm{off}} \\
0 & 0 & 0 & 0 & \eta_{xy}^{\mathrm{B}} & \pi J & 0 & -k_{\mathrm{on}}^{\mathrm{app}} & 0 & 0 & R_2^{\mathrm{B},1} & \Omega^{\mathrm{B}} & -\omega_y \\
0 & 0 & 0 & 0 & -\pi J & \eta_{xy}^{\mathrm{B}} & 0 & 0 & -k_{\mathrm{on}}^{\mathrm{app}} & 0 & -\Omega^{\mathrm{B}} & R_2^{\mathrm{B},1} & \omega_x \\
0 & 0 & 0 & 0 & 0 & 0 & \eta_z^{\mathrm{B}} & 0 & 0 & -k_{\mathrm{on}}^{\mathrm{app}} & \omega_y & -\omega_x & R_1^{\mathrm{B}}+\rho_{\mathrm{HH}}^{\mathrm{B}}+k_{\mathrm{off}}
\end{bmatrix}
\begin{bmatrix} E/2 \\ I_x^{\mathrm{A}} \\ I_y^{\mathrm{A}} \\ I_z^{\mathrm{A}} \\ I_x^{\mathrm{B}} \\ I_y^{\mathrm{B}} \\ I_z^{\mathrm{B}} \\ 2I_x^{\mathrm{A}}H_{\mathrm{Z}}^{\mathrm{A}} \\ 2I_y^{\mathrm{A}}H_z^{\mathrm{A}} \\ 2I_z^{\mathrm{A}}H_z^{\mathrm{A}} \\ 2I_x^{\mathrm{B}}H_z^{\mathrm{B}} \\ 2I_y^{\mathrm{B}}H_z^{\mathrm{B}} \\ 2I_z^{\mathrm{B}}H_z^{\mathrm{B}} \end{bmatrix}, \quad \textbf{[S10]}$$

where $R_2^{\mathrm{A},1}=R_2^{\mathrm{A,0,in\text{-}phase}}+\rho_{\mathrm{HH}}^{\mathrm{A}}+k_{\mathrm{on}}^{\mathrm{app}}$ and $R_2^{\mathrm{B},1}=R_2^{\mathrm{B,0,in\text{-}phase}}+\rho_{\mathrm{HH}}^{\mathrm{B}}+k_{\mathrm{off}}$; η_{xy}^{A} and η_{xy}^{B} are the transverse cross-correlated relaxation rates in states A and B, respectively; η_z^{A} and η_z^{B} are the longitudinal cross-correlated relaxation rates in states A and B, respectively; and J is ${}^1J_{\mathrm{NH}}$ = 92 Hz. The cross-correlated terms are only included in Eq. **S10** for completeness, because they are suppressed in the DEST experiment by the application of a 180° ^{1}H pulse every 100 ms during the ^{15}N CW saturation period. In addition, the approximations $R_2(2I_{xy}H_z) \cong R_2(I_{xy}) + \rho_{\mathrm{HH}}$ and $R_1(2I_zH_z) \cong R_1(I_z) + \rho_{\mathrm{HH}}$ are made because for a given state, ρ_{HH} should be the same in $R_2(2I_{xy}H_z)$ and $R_1(2I_zH_z)$. The time course of the magnetization explicitly incorporating both in-phase and antiphase terms can then be simulated. For state A (the free state), ρ_{HH} was calculated for each residue using the formula $2(R_2^{\mathrm{CPMG}}-R_2^{\mathrm{in\text{-}phase}})$, where R_2^{CPMG} and $R_2^{\mathrm{in\text{-}phase}}$ were experimentally measured on free Aβ (in the absence of GroEL). For state B (the bound state), $R_2^{\mathrm{in\text{-}phase}}$ was estimated by $R_2^{\mathrm{CPMG}}/\gamma$, where γ is the empirically determined slope of the correlation plot between $R_2^{\mathrm{CPMG,bound}}$ and $R_2^{\mathrm{in\text{-}phase,bound}}$, and ρ_{HH} was estimated by $2R_2^{\mathrm{CPMG}}(\gamma-1)/\gamma$. At 900 MHz, γ = 1.12 (Fig. S6*B*).

Numerical simulations show that Eq. **S2** is sufficient, because the simulated DEST profiles calculated using Eq. **S2** or Eq. **S10** are effectively indistinguishable (Fig. S7*A*). Even the DEST profiles calculated using Eq. **S2** with either $R_2^{\mathrm{in\text{-}phase}}$ or R_2^{CPMG} differ minimally, and these differences are well within the experimental uncertainties in the measured cross-peak intensities as a function of the frequency offset of the ^{15}N saturation pulse (Fig. S7*B*). Global simultaneous fitting to all the DEST, $\Delta R_2^{\mathrm{CPMG}}$, CPMG relaxation dispersion, and exchange-induced shift data resulted in no significant differences in the fitted parameters for any give case: (*i*) explicitly including in-phase and antiphase terms in fitting to the DEST data (Eq. **S10**); (*ii*) simply assuming transverse relaxation rates in the free and bound states are represented by the optimized residue-specific values for $R_2^{\mathrm{CPMG,bound}}$ directly; or (*iii*) substituting measured in-phase values for the free relaxation rate and scaling the $R_2^{\mathrm{CPMG,bound}}$ parameter by $1/\gamma$ in the DEST fitting to account for slightly slower in-phase relaxation.

Numerical Simulation of Exchange-Induced Shifts in Real-Time and CT NMR Experiments. ^{13}Cα and ^{13}Cβ ^{13}C chemical shifts were indirectly recorded using a 56-ms CT period, thereby eliminating the $^{1}J_{\mathrm{CC}}$ evolution for improved spectral resolution that is crucial for this study. We note, however, that Eq. **S6** for the exchange-induced shift (18) was derived for the case of real-time evolution. The potential impact of the CT delay on the exchange-induced shift therefore needed to be assessed before the ^{13}C chemical shift changes observed for Aβ40 in the presence of GroEL could be analyzed using this equation. To this end, numerical simulations of both real-time and CT spectra were performed based on the equation (18):

$$\frac{d}{dt}\begin{bmatrix} V_{\mathrm{A}}(t) \\ V_{\mathrm{B}}(t) \end{bmatrix} = \begin{bmatrix} -i\omega_{\mathrm{A}} - k_{\mathrm{on}}^{\mathrm{app}} - R_2^{\mathrm{A},0} & k_{\mathrm{off}} \\ k_{\mathrm{on}}^{\mathrm{app}} & -i\omega_{\mathrm{B}} - k_{\mathrm{off}} - R_2^{\mathrm{B},0} \end{bmatrix} \begin{bmatrix} V_{\mathrm{A}}(t) \\ V_{\mathrm{B}}(t) \end{bmatrix}, \qquad \textbf{[S11]}$$

where $V_{\mathrm{A}}(t)$ and $V_{\mathrm{B}}(t)$ are the amounts of coherence V in the A (free) and B (GroEL-bound) states at time t; ω_{A} and ω_{B} are the corresponding Zeeman frequencies in radians·s^{-1}; $k_{\mathrm{on}}^{\mathrm{app}}$ and k_{off} are the pseudo–first-order on-rate and off-rate, respectively (corresponding to the transition from A to B and from B to A, respectively); and $R_2^{\mathrm{A},0}$ and $R_2^{\mathrm{B},0}$ are the corresponding transverse spin relaxation rates in the absence of exchange (18).

The solution to the above equation for the real-time experiment can be written as follows:

$$\begin{bmatrix} V_{\mathrm{A}}(t) \\ V_{\mathrm{B}}(t) \end{bmatrix} = \exp\left(\begin{bmatrix} -i\omega_{\mathrm{A}} - k_{\mathrm{on}}^{\mathrm{app}} - R_2^{\mathrm{A},0} & k_{\mathrm{off}} \\ k_{\mathrm{on}}^{\mathrm{app}} & -i\omega_{\mathrm{B}} - k_{\mathrm{off}} - R_2^{\mathrm{B},0} \end{bmatrix} t \right) \times \begin{bmatrix} V_{\mathrm{A}}(0) \\ V_{\mathrm{B}}(0) \end{bmatrix}, \qquad \textbf{[S12]}$$

with initial conditions $V_{\mathrm{A}}(0) = k_{\mathrm{off}}/(k_{\mathrm{on}}^{\mathrm{app}} + k_{\mathrm{off}})$ and $V_{\mathrm{B}}(0) = k_{\mathrm{on}}^{\mathrm{app}}/(k_{\mathrm{on}}^{\mathrm{app}} + k_{\mathrm{off}})$ for a two-state chemical exchange process in equilibrium. The matrix exponential in Eq. **S12** can be numerically evaluated using the matrix exponential function within MATLAB, which allows the real-time spectrum $F_{\mathrm{A}}^{\mathrm{RT}}$ in the free state to be obtained by Fourier transformation of $V_{\mathrm{A}}(t)$.

For the CT spectrum with a CT period of $2T$, $F_{\mathrm{A}}^{\mathrm{CT}}$ in the free state is acquired at $T + t/2$ and $T - t/2$ before and after the refocusing ^{13}C pulse, respectively. We first used Eq. **S12** and associated initial conditions to calculate both $V_A(T + t/2)$ and $V_B(T + t/2)$ (i.e., the amounts of coherence V in the free and bound states at time point $T + t/2$, immediately before the refocusing pulse). The subsequent 180° pulse with phase x flips the sign of the y component of coherence V, and its effect can be simply represented by taking the complex conjugate of $V_{\mathrm{A}}(T + t/2)$ and $V_{\mathrm{B}}(T + t/2)$. The complex conjugate of these two terms is then used as the new initial condition to replace $V_{\mathrm{A}}(0)$ and $V_{\mathrm{B}}(0)$ in Eq. **S12**, which computes the additional evolution of coherence V during the time $T - t/2$. The overall CT evolution of coherence V is thus formulated as follows:

$$\begin{bmatrix} V_{\mathrm{A}}(t) \\ V_{\mathrm{B}}(t) \end{bmatrix} = \exp\left(\begin{bmatrix} -i\omega_{\mathrm{A}} - k_{\mathrm{on}}^{\mathrm{app}} - R_2^{\mathrm{A},0} & k_{\mathrm{off}} \\ k_{\mathrm{on}}^{\mathrm{app}} & -i\omega_{\mathrm{B}} - k_{\mathrm{off}} - R_2^{\mathrm{B},0} \end{bmatrix} (T - t/2) \right) conj\left(\exp\left(\begin{bmatrix} -i\omega_{\mathrm{A}} - k_{\mathrm{on}}^{\mathrm{app}} - R_2^{\mathrm{A},0} & k_{\mathrm{off}} \\ k_{\mathrm{on}}^{\mathrm{app}} & -i\omega_{\mathrm{B}} - k_{\mathrm{off}} - R_2^{\mathrm{B},0} \end{bmatrix} (T + t/2) \right) \begin{bmatrix} V_{\mathrm{A}}(0) \\ V_{\mathrm{B}}(0) \end{bmatrix} \right), \qquad \textbf{[S13]}$$

where *conj* stands for taking the complex conjugate of each term in the resulting column vector. Fourier transformation of the final coherence in the free state $V_{\mathrm{A}}(t)$ then yields the CT spectrum $F_{\mathrm{A}}^{\mathrm{CT}}$.

Numerical simulations were performed in MATLAB using a CT delay $2T$ of 56 ms, with values of $k_{\mathrm{on}}^{\mathrm{app}}$ and k_{off} of 34.8 and 1,440 s^{-1}, as determined in the main text, and a range of appropriate ^{13}C-R_2 values in the free (12.5–16.5 s^{-1}) and bound (520–1,740 s^{-1}) states derived from the backbone ^{15}N-R_2 rates determined from global fitting in the main text. Using a spectral width of 400 Hz, the evolution of $V_{\mathrm{A}}(t)$ in both real-time and CT experiments was calculated from $t = 0$ to 56 ms in intervals of 2.5 ms, apodized using a cosine window function, and zero-filled to 2,048 points before Fourier transformation to obtain the real-time $F_{\mathrm{A}}^{\mathrm{RT}}$ and CT $F_{\mathrm{A}}^{\mathrm{CT}}$ spectra. The point with the highest intensity in each spectrum was first picked, and together with the immediately adjacent points on the upfield and downfield sides, was best-fitted to a parabolic function whose maximum is then determined as the observed peak position of the free state. This approach provides a much more accurate peak position than the direct pick of the most intense point when the simulated time domain data are only moderately zero-filled. The exchange-induced shift is then obtained from the difference between the simulated peak position and $\omega_{\mathrm{A}}/2\pi$ (−100 Hz used throughout the simulations, whereas the frequency for the bound B state varied from −82 to 105 Hz). Within the range of relaxation and exchange parameters observed in our study, we found that the difference between the exchange-induced shifts observed in the real-time and CT experiments was less than 2% (i.e., around 0.02 Hz for a 1.0-Hz exchange-induced shift), smaller than the experimental accuracy attainable for this type of measurement in our study. The simulated shifts in the two experiments are essentially the same as the value calculated using the analytical expression given by Eq. **S6**, thereby validating the use of Eq. **S6** for the analysis of exchange-induced shifts in CT spectra over the range of conditions applicable to the current study.

Calculating ^{1}H$_{\mathrm{N}}$ Chemical Shifts for GroEL-Bound Aβ40. The ^{1}H$_{\mathrm{N}}$ exchange-induced shifts were measured from the same spectra used to determine the ^{15}N exchange-induced shifts. The ^{1}H$_{\mathrm{N}}$-R_2 measurements were carried out as described previously (5). Given the experimental ^{1}H$_{\mathrm{N}}$-R_2 values in the absence and presence of GroEL, the ^{1}H$_{\mathrm{N}}$-R_2 values in the GroEL-bound form were determined by nonlinear least-squares minimization of the difference between observed and calculated (from Eqs. **S2** and **S3**) ^{1}H$_{\mathrm{N}}$-ΔR_2 values, optimizing the ^{1}H$_{\mathrm{N}}$-R_2 values in the GroEL-bound state while holding fixed the global rate constant parameters derived from the ^{15}N data and the experimental ^{1}H$_{\mathrm{N}}$-R_2 values in the free state. With the calculated ^{1}H$_{\mathrm{N}}$-R_2 values for the GroEL-bound form and the experimental exchange-induced ^{1}H$_{\mathrm{N}}$ shifts in hand, the ^{1}H$_{\mathrm{N}}$ chemical shift differences between the GroEL-bound and free forms of Aβ40 were calculated using Eq. **S6** (with ^{1}H$_{\mathrm{N}}$ shifts replacing ^{15}N shifts) solved for $\Delta\omega$.

Calculating ^{13}Cα and ^{13}Cβ Chemical Shifts for GroEL-Bound Aβ40. The ^{13}Cα and ^{13}Cβ shifts in the GroEL-bound state were calculated from the corresponding experimental exchange-induced ^{13}C shifts and calculated $^{13}\text{C-}R_2$ values for the GroEL-bound state, using Eq. **S6** (with ^{13}C shifts replacing ^{15}N shifts), as described for the $^{1}\text{H}_\text{N}$ shifts above. The $^{13}\text{C-}R_2$ values in the GroEL-bound state, however, could not be determined experimentally because the broadness of the cross-peaks in the CT-HSQC spectrum precluded the making of accurate $^{13}\text{C-}R_2$ measurements in the presence of GroEL. The ^{13}Cα and ^{13}Cβ R_2 values in the GroEL-bound state were therefore calculated directly from the corresponding $^{15}\text{N-}R_2$ values taking into account the different gyromagnetic ratios of ^{13}C and ^{15}N and the different N-H and C-H bond lengths (see below). This approach is justified because motion of N-H and Cα-H vectors of a given residue will be virtually identical, and $^{13}\text{C-}R_2$ measurements on free Aβ40 indicate that the ratio of ^{13}Cβ to ^{13}Cα R_2 values of the same residue is ∼0.9, with the exception of the alanine methyl groups, where the apparent ratio is close to 0.5.

As noted above, the calculation of bound ^{13}C chemical shifts requires the values of $^{13}\text{C-}R_2^{\text{CPMG,bound}}$ to be known. At 900 MHz, the ratio $(\alpha)^{13}\text{C-}R_2^{\text{in-phase,bound}}/^{15}\text{N-}R_2^{\text{in-phase,bound}}$ (assuming the same order parameter for the N-H and Cα-H bond vectors within a given residue) is calculated to be 2.7, based on the known values of N-H and C-H bond lengths, as well as the gyromagnetic ratios and chemical shift anisotropies of ^{13}C and ^{15}N. Assuming to a first approximation that the proton density surrounding H_N, Hα, and Hβ is the same, such that the R_ext term (see Eq. **S8**) has roughly the same value for ^{15}N, ^{13}Cα, and ^{13}Cβ, $^{13}\text{C-}R_2^{\text{CPMG,bound}}$ at 900 MHz can be readily calculated from $^{15}\text{N-}R_2^{\text{CPMG,bound}}$ at 900 MHz using the equation:

$$^{13}\text{C-}R_2^{\text{CPMG,bound}} = \lambda\,^{15}\text{N-}R_2^{\text{CPMG,bound}}[(\alpha+\gamma-1)/\gamma], \qquad \textbf{[S14]}$$

where λ is the ratio of the ^{13}C- to ^{15}N-order parameters $S^2_\text{C}/S^2_\text{N}$ with values of 1, 0.9, and 0.5 (see above) for ^{13}Cα, ^{13}Cβ, and ^{13}Cβ-methyl, respectively, and γ is the ratio of $^{15}\text{N-}R_2^{\text{CPMG,bound}}$ to $^{15}\text{N-}R_2^{\text{in-phase,bound}}$, which is equal to 1.12 at 900 MHz (Fig. S6*B*).

Average End-to-End Distance Between the Centers of the Two GroEL-Binding Aβ40 Hydrophobic Regions. From both the experimental $^{15}\text{N-}\Delta R_2$ data (Fig. 1*A*) and the computed $^{15}\text{N-}R_{2,\text{calc}}^{\text{GroEL-bound}}$ values (Fig. 4*A*), one can conclude that the centers of the two main GroEL-binding hydrophobic regions are located at residues 19 and 32. For a random coil, the expected average rms end-to-end distance $\langle r^2\rangle_0^{1/2}$ between residues 19 and 32 is expected to lie between 32 and 38 Å, calculated from $\langle r^2\rangle_0^{1/2} = (C_n n l^2)^{1/2}$, where l is the Cα-Cα distance (3.8 Å), n is the number of residues (14 in this instance), and C_n is the characteristic ratio (estimated to be between 5 and 7 for a polypeptide of n = 14 with only one glycine) (20).

1. Fawzi NL, Ying J, Ghirlando R, Torchia DA, Clore GM (2011) Atomic-resolution dynamics on the surface of amyloid-β protofibrils probed by solution NMR. *Nature* 480(7376):268–272.
2. Iwahara J, Anderson DE, Murphy EC, Clore GM (2003) EDTA-derivatized deoxythymidine as a tool for rapid determination of protein binding polarity to DNA by intermolecular paramagnetic relaxation enhancement. *J Am Chem Soc* 125(22): 6634–6635.
3. Grason JP, Gresham JS, Lorimer GH (2008) Setting the chaperonin timer: A two-stroke, two-speed, protein machine. *Proc Natl Acad Sci USA* 105(45): 17339–17344.
4. van der Vies SM, Viitanen PV, Gatenby AA, Lorimer GH, Jaenicke R (1992) Conformational states of ribulosebisphosphate carboxylase and their interaction with chaperonin 60. *Biochemistry* 31(14):3635–3644.
5. Fawzi NL, Ying J, Torchia DA, Clore GM (2010) Kinetics of amyloid β monomer-to-oligomer exchange by NMR relaxation. *J Am Chem Soc* 132(29):9948–9951.
6. Lakomek NA, Ying JF, Bax A (2012) Measurement of ^{15}N relaxation rates in perdeuterated proteins by TROSY-based methods. *J Biomol NMR* 53(3):209–221.
7. Yip GN, Zuiderweg ER (2004) A phase cycle scheme that significantly suppresses offset-dependent artifacts in the R_2-CPMG ^{15}N relaxation experiment. *J Magn Reson* 171(1):25–36.
8. Delaglio F, et al. (1995) NMRPipe: A multidimensional spectral processing system based on UNIX pipes. *J Biomol NMR* 6(3):277–293.
9. Kontaxis G, Clore GM, Bax A (2000) Evaluation of cross-correlation effects and measurement of one-bond couplings in proteins with short transverse relaxation times. *J Magn Reson* 143(1):184–196.
10. Santoro J, King GC (1992) A constant-time 2D Overbodenhausen experiment for inverse correlation of isotopically enriched species. *J Magn Reson* 97(1):202–207.
11. Vuister GW, Bax A (1992) Resolution enhancement and spectral editing of uniformly ^{13}C-enriched proteins by homonuclear broad-band ^{13}C decoupling. *J Magn Reson* 98: 428–435.
12. Kay LE, Keifer P, Saarinen T (1992) Pure absorption gradient enhanced heteronuclear single quantum correlation spectroscopy with improved sensitivity. *J Am Chem Soc* 114:10663–10665.
13. Baldwin AJ, Kay LE (2012) Measurement of the signs of methyl ^{13}C chemical shift differences between interconverting ground and excited protein states by $R_{1\rho}$: An application to αB-crystallin. *J Biomol NMR* 53(1):1–12.
14. McConnell HM (1958) Reaction rates by nuclear magnetic resonance. *J Chem Phys* 28(3):430–431.
15. Helgstrand M, Härd T, Allard P (2000) Simulations of NMR pulse sequences during equilibrium and non-equilibrium chemical exchange. *J Biomol NMR* 18(1):49–63.
16. Fawzi NL, Ying J, Torchia DA, Clore GM (2012) Probing exchange kinetics and atomic resolution dynamics in high-molecular-weight complexes using dark-state exchange saturation transfer NMR spectroscopy. *Nat Protoc* 7(8):1523–1533.
17. Palmer AG, 3rd, Kroenke CD, Loria JP (2001) Nuclear magnetic resonance methods for quantifying microsecond-to-millisecond motions in biological macromolecules. *Methods Enzymol* 339:204–238.
18. Skrynnikov NR, Dahlquist FW, Kay LE (2002) Reconstructing NMR spectra of "invisible" excited protein states using HSQC and HMQC experiments. *J Am Chem Soc* 124(41):12352–12360.
19. Loria JP, Rance M, Palmer AG (1999) A relaxation-compensated Carr-Purcell-Meiboom-Gill sequence for characterizing chemical exchange by NMR spectroscopy. *J Am Chem Soc* 121:2331–2332.
20. Cantor CR, Schimmel PR (1980) *The Behavior of Biological Macromolecules, Part III* (Freeman, San Francisco).

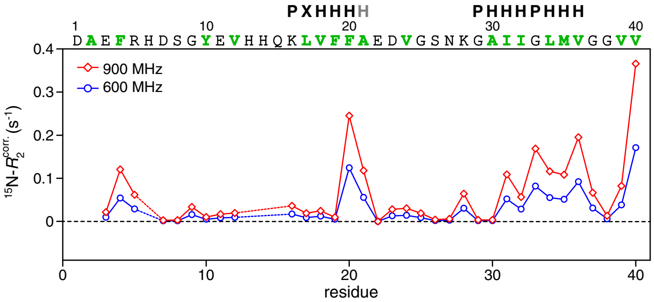

Fig. S1. Chemical exchange line-broadening correction factors used for the ^{15}N-ΔR_2 data. The ^{15}N-ΔR_2 measurements were carried out at a CPMG field of 550 Hz. At this field strength, there is minimal chemical exchange-induced line-broadening in the presence of GroEL. The correction (corr.) factors plotted are the contributions from chemical exchange line-broadening at a CPMG field of 550 Hz in the presence of 20 μM GroEL derived from fitting the ^{15}N relaxation dispersion measurements (*SI Materials and Methods*). The contribution of exchange line-broadening to ΔR_2 is negligible compared with the lifetime line-broadening effect (up to ~25 s^{-1}) arising from the very large R_2 values when Aβ40 is bound to GroEL, leading to very rapid decay of magnetization of Aβ40 resonances in the bound state. The fact that exchange line-broadening is negligible compared with lifetime line-broadening is further evidenced by the observation that ΔR_2 is completely uncorrelated to the small but observable chemical exchange-induced ^{15}N shifts in the presence of GroEL (Fig. 2*E*).

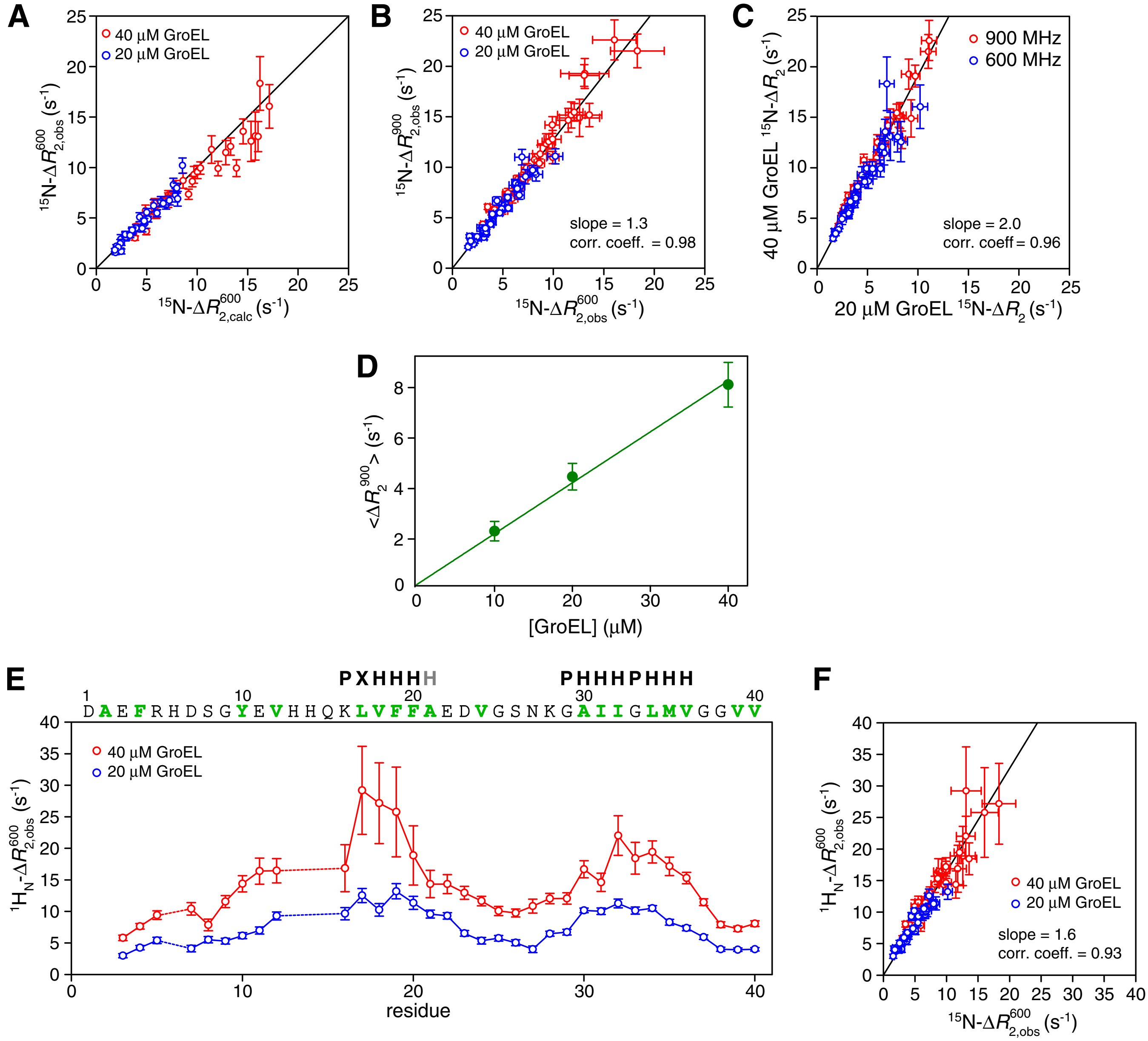

Fig. S2. ΔR_2 measurements. ΔR_2 is given by the difference in R_2 for Aβ40 in the presence and absence of GroEL. (*A*) Correlation between observed (obs) and calculated (calc) ^{15}N-ΔR_2 values at a spectrometer frequency of 600 MHz. (*B*) Correlation between observed ^{15}N-ΔR_2 values at spectrometer frequencies of 900 and 600 MHz. corr. coeff., correlation coefficient. (*C*) Correlation between observed ^{15}N-ΔR_2 values in the presence of 20 and 40 μM GroEL. (*D*) Average ^{15}N-ΔR_2 as a function of GroEL concentration at a spectrometer frequency of 900 MHz. (*E*) ^{1}H$_N$-ΔR_2 values at 600 MHz in the presence of 20 (blue) and 40 (red) μM GroEL. (*F*) Correlation between ^{1}H$_N$-ΔR_2 and ^{15}N-ΔR_2 values. Error bars = 1 SD.

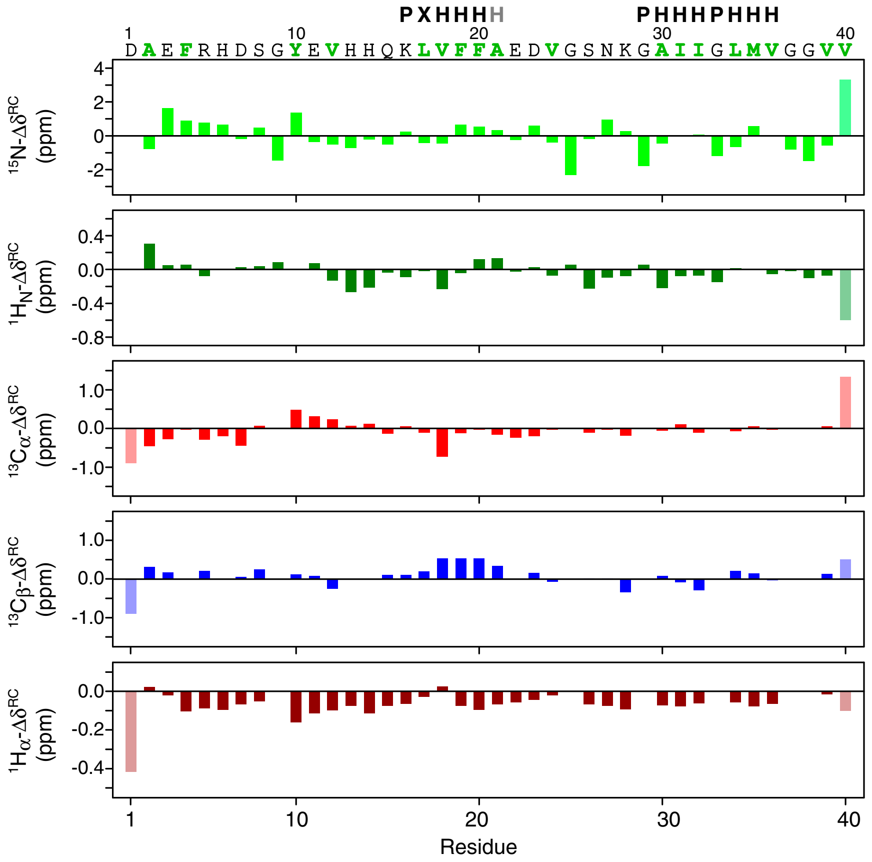

Fig. S3. Deviations ($\Delta\delta^{RC}$) of ^{15}N, ^{1}H$_N$, ^{13}Cα, ^{13}Cβ and ^{1}Hα chemical shifts of free Aβ40 (50 μM and 5 °C) from random coils. The random coil (RC) shifts are those recently published by Kjaergaard and Poulsen (1) that incorporate neighbor correction factors, and the deviations from random coil shifts were calculated using the Web server http://spin.niddk.nih.gov/bax/nmrserver/Poulsen_rc_CS. The bars for the terminal residues 1 and 40 that are shaded as the larger deviations from random coil shifts are due to end effects.

1. Kjaergaard M, Poulsen FM (2011) Sequence correction of random coil chemical shifts: Correlation between neighbor correction factors and changes in the Ramachandran distribution. *J Biomol NMR* 50(2):157–165.

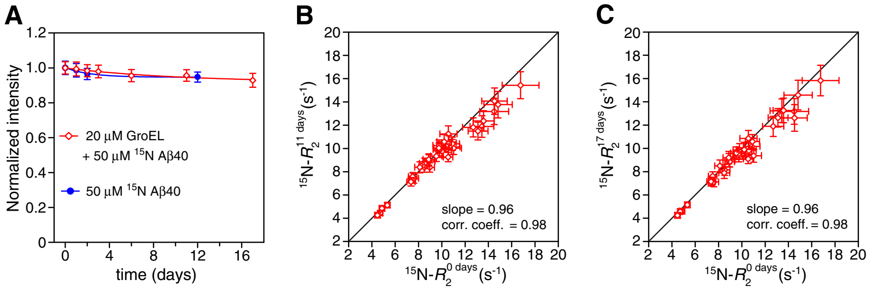

Fig. S4. Stability of Aβ40 samples in the presence of GroEL. *(A)* Average normalized ^{1}H$_N$-^{15}N cross-peak intensity as a function of time. There is a very small decrease in intensity (<5%) in the first 2 d; thereafter, the sample remains stable. Correlation of measured ^{15}N-R_2 values at time 0 with the corresponding values measured after 11 (*B*) and 17 (*C*) d, respectively, at a spectrometer frequency of 600 MHz in the presence of 20 μM GroEL. Error bars = 1 SD.

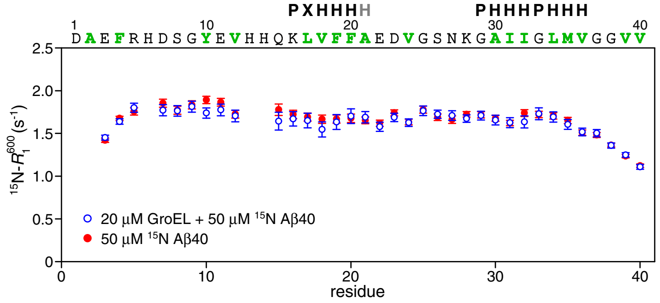

Fig. S5. ^{15}N-R_1 in the presence (blue) and absence (red) of GroEL.

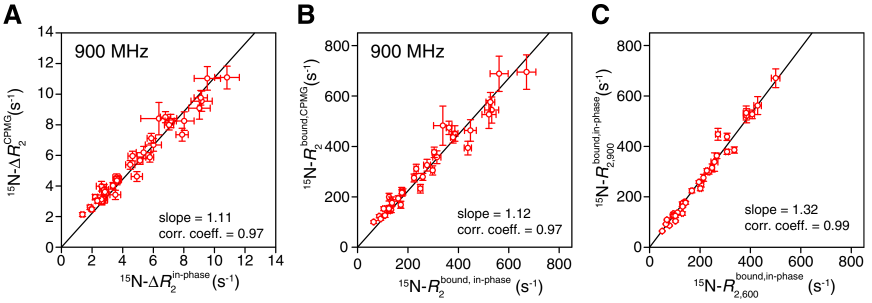

Fig. S6. Correlation between R_2 values measured from CPMG (average of in-phase and antiphase R_2) and $R_{1\rho}$ (in-phase). Correlation between measured ^{15}N-ΔR_2^{CPMG} and $\Delta R_2^{\text{in-phase}}$ values at 900 MHz (*A*), calculated $R_2^{\text{CPMG, bound}}$ and $R_2^{\text{in-phase, bound}}$ values at 900 MHz (*B*), and calculated $R_2^{\text{in-phase, bound}}$ values at 900 and 600 MHz (*C*).

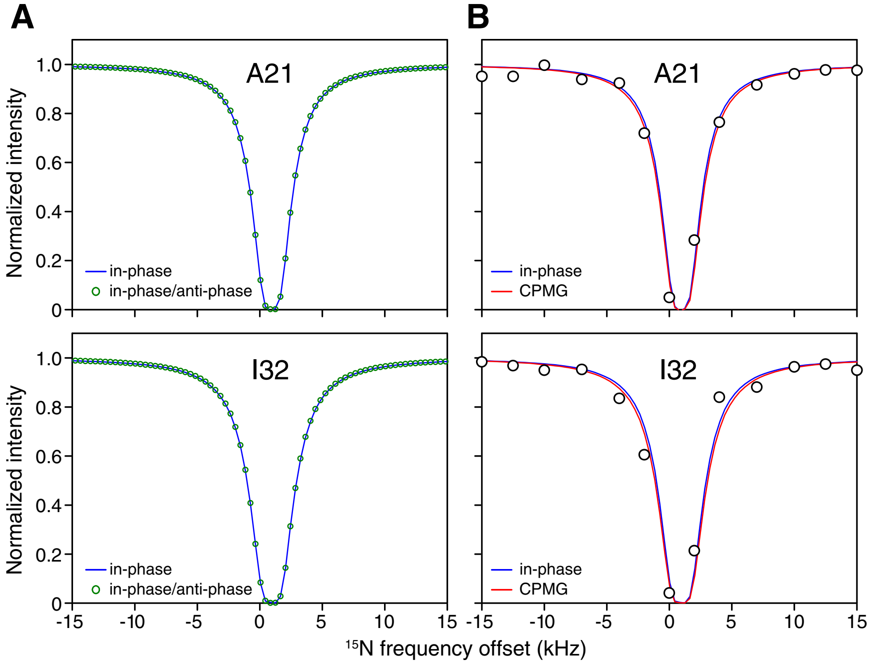

Fig. S7. Impact of R_2 values on the DEST profiles of two residues: Ala21 (A21) and Ile32 (I32). (*A*) DEST profiles for Ala21 (*Upper*) and Ile32 (*Lower*) calculated using Eq. **S2** with R_2 set to $R_2^{\text{in-phase}}$ (blue line) and the expanded description provided by Eq. **S10**, which makes use of both in-phase and antiphase R_2 terms (green circles). The DEST profiles are indistinguishable, indicating that any antiphase magnetization created during the ^{15}N CW saturation pulse is minimal. (*B*) Comparison of the DEST profiles calculated using Eq. **S2** with R_2 set to either $R_2^{\text{in-phase}}$(blue line) or R_2^{CPMG}(red line) with the experimental DEST profiles (black open circles).